Fatigue crack growth under large scale yielding condition: The need of a characteristic length scale

Vincent Maurel, Alain Köster, Luc Rémy, Matthieu Rambaudon, Djamel Missoum-Benziane, Vincent Fontanet, Flora Salgado Goncalves, Auréliane Heudt, H. Wang, Mariem Trabelsi

Fatigue crack growth under large scale yielding condition: the need of a characteristic length scale

V. Maurel[a,1], A. Köster[a], L. Rémy[a], M. Rambaudon[a], D. Missoum-Benziane[a], V. Fontanet[a], F. Salgado-Goncalves[a], A. Heudt[a], H. Wang[b], M. Trabelsi[a]

[a] *MINES ParisTech, PSL Research University, MAT - Centre des Matériaux, CNRS UMR 7633, BP 87 91003 Evry, France*

[b] *Département Calculs Mécaniques du Solide - Turbomachines, Safran Engineering Services, SAFRAN - Etablissement PARIS-SACLAY, Rue des Jeunes Bois, CS80112, 78772 Magny-les-Hameaux*

Abstract

Fatigue crack growth under large scale yielding condition is studied for a commercial base Co superalloys, Haynes® 188, for single edge notch (SENT) specimen. Due to very high temperature and applied strain values, it is observed that major crack interacts with micro-cracks pattern. These micro-cracks are found to be associated to strain localization and local high triaxiality stress ratio. Detailed analysis of strain localization and stress concentration was used to define an optimal characteristic length used in a non-local modeling of strain energy involved in crack growth process. To obtain robust and low time consuming crack growth modeling, a post-processing methodology is thus proposed for fatigue crack growth under large scale yielding. This point was successfully achieved for SENT specimen test series to describe crack growth rate. Finally, test driven for another geometry has enabled to validate the proposed modeling methodology.

Keywords: Low cycle fatigue, Strain energy method, High temperature fatigue, Non-local model, In situ observation

*Corresponding author. Tel.: +33-1-60 76 30 03; Fax: +33-1-60 76 31 50
E-mail address: vincent.maurel@mines-paristech.fr

1. Introduction

For components used at high temperature and bearing very high loading, fatigue failure could be induced by crack growth in few tenths or hundreds of cycles. Nevertheless, the increasing demand on shape and weight optimization for industrial parts, push the need of an increasing knowledge in the field of fatigue crack growth and its assessment under Low Cycle Fatigue (LCF) loading conditions. Fatigue crack growth is for metallic materials associated to dislocations pile-up at the crack tip [1, 2] and subsequent crack tip blunting [3, 4]. Thus strain localization at the crack tip is known to play a crucial role in fatigue crack growth rate (FCGR). For small scale yielding condition, plasticity has been observed to be confined to microscopic volume more or less function of grain size of the studied material [5]. This point is often described as a process zone where fatigue damage will progressively lead to local material failure and crack growth [6, 7, 8]. For increasing applied loading, the size of the volume of matter where significant plasticity occurs increases and could affect multiple grains with or without influence of their orientation in a "mesoscopic" volume [9]. As a consequence of the increase in plasticity, and especially within the strain localization path, it appears a strong correlation between distribution of plasticity level and micro-cracks density and size [10, 11]. Thus large scale yielding condition induces a loss of confinement of the plastic volume and raises the question of the size of the process zone.

The use of finite element analysis (FEA) is required to analyze carefully local loading and FCGR. It has been shown that for single crystal under small scale yielding condition, a local approach, defined in a post-processor, is straightforward to assess fatigue crack growth rate without explicit remeshing of the growing crack [12]. These kind of approaches are known to induce mesh dependency which drawback could be overcame using J integral enabling the direct use of linear elastic fracture mechanics, especially Paris-like models based on stress intensity factor (SIF) analysis and its extension to J integral [13, 14, 15, 16]. But for large applied strain level, it is no more possible to determine an integration path without influence of the chosen path, making J approaches out of rules of use and inoperative due to the loss of their invariance with integration path. For large scale yielding condition, one can differentiate plastic strain accommodation occurring in overload condition from cyclic hardening. The case of overload effect, leading to a plastic volume where crack grows with no significant plastic extent, has been widely commented [17] and efficiently modeled using for instance J integral for retardation effect observed for long crack as well as for short crack analysis [18, 19]. In this case, the crack grows in a hardened and/or damaged material without large modification of this state before new overload cycle. However, for crack growth leading to a sustained cyclic hardening of the un-cracked material, some recent works have proposed the used of incremental elastic-plastic integral to take into account elastic-plastic material behavior for ductile failure and its extension to cyclic plasticity [20, 21]. Nevertheless, the authors have stressed out that elastic-plastic integral was still path dependent. The proposed configurational forces

method was seen to be straightforward to ensure path independence only for limited plastic zone size. As a conclusion, the path should embrace the cyclic plastic zone, leading to a strong influence of back face plasticity when considering for instance CT specimen [21].

Considering crack initiation criteria for life modeling in the range of low cycle fatigue, it has been clearly shown that plastic dissipation, that could be assessed by inelastic strain energy density, is fully relevant to account for complex loading including multiaxiality effect and/or non isothermal condition [22, 23, 24]. Considering fatigue crack growth model in the range of low cycle fatigue, the FCGR model proposed by Mc Clintock has shown its efficiency for sustained plasticity [6, 25, 12]. Recently, some authors have proposed to make a link between plastic energy and fatigue crack growth for small scale yielding condition [26, 27] as well as for large scale yielding condition [28]. It is worth noting that the transition between very low cycle fatigue (tenths of cycles) to the end of LCF domain ($N_f \simeq 10^5$) needs to account for both elastic and plastic energy as described in [29] for life assessment and in [28] for fatigue crack growth modeling. In this study, FCGR was successfully modeled using strain energy obtained from macroscopic stress-strain evolution. This strain energy was deduced from experimental measurement of global force and extensometer strain values respectively, or finite elements modeling of the experiment using the same macroscopic values without analysis of the stress/strain gradients in the specimen. This model was also reliable to assess life of smooth specimen, but needs a careful investigation of the modification of stress/gradient induced by the modification of the geometry. In the case of short fatigue crack growth for single crystal superalloys, combining the energy partition proposed in [28] with critical distance concept [30] was seen to provide good results for fatigue crack growth rate modeling of notched specimen, and associated strain gradient, as well as for life assessment of plain specimens [31]. Early works have also proposed to account for varying size of analysis (i.e. size of strain averaging) to account for large scale yielding in the scope of process zone based model [8].

Nevertheless, the high level of plastic increment observed at each cycle makes large scale yielding for fatigue close to monotonic crack growth observed for ductile material. Thus, it is needed to have a close look at damage induced by stress triaxiality, since the increase of stress triaxiality is known to reduce the strain to failure of most ductile materials [32]. Damage modeling could be thus coupled with the stress triaxiality [33] since it greatly impacts the damage rate as observed for extension of Gurson-like models for low cycle fatigue [34]. In the context of the modeling of ductile failure, many authors have shown that non-local approach could overcome mesh dependency introducing a characteristic length of the material and of the damage mechanism to be analyzed [35, 36, 37, 38]. Considering life assessment for multiaxial fatigue in small scale yielding condition, non-local approaches have also provided excellent results [39]. In the context of fatigue under large scale yielding, the correlation of large volume of cyclic plasticity and process zone makes non-local approach as a good candidate for robust modeling of fatigue

crack growth.

For high temperature application, both Ni and Co based superalloys are used for instance in combustion chambers. This study is devoted to the analysis of the Co based superalloy Haynes® 188 commercial material. This material was deeply analysed concerning low cycle fatigue testing performed on smooth specimens [40, 41, 42, 43] exhibiting a strong cyclic hardening at intermediate temperatures due to dynamic strain aging but with limited effect at high temperature (above 800°C) [44, 45]. Crack growth studies are mostly related to small scale yielding conditions for this material using CT specimen [46]. Moreover, it is observed a large influence of hold time for isothermal fatigue tests performed at high temperature (above 800°C) for either LCF tests, achieved up to smooth specimen failure, or crack growth analysis [41, 47, 48, 43]. It is worth noting that, most models accounting for this kind of creep/fatigue interactions are addressed for the time being by rules of cumulative damage [49, 50] without explicit use of FCGR. It has also been clearly evidenced that both number of cycles to failure and fatigue crack growth rate are function of temperature and environment [51, 52]. At high temperature, oxidation could strongly interact with fatigue crack growth due to the enhancement of oxidation kinetics under local plasticity under fatigue [53, 54] or creep [55]. Thus, the high temperature testing in air is clearly more damaging than vacuum testing [53, 51].

Development of SEM in situ testing has provided significant progress in the understanding of crack growth mechanisms and localization phenomena based on digital image correlation technique [56, 57, 58, 59]. Recent progress in optical devices, allowing for in situ surface monitoring with spatial resolution close to SEM in situ devices, could also provide the same kind of informations but with no specific modification of the testing methodology. This "non-intrusive" approach allows to test standard specimen and/or robust experimental configuration according to the tested representative element volume (R.E.V.) [60, 61, 62].

This paper will study both experimental and modeling issues of fatigue crack growth under large scale yielding condition for the chosen Co base superalloy. The experimental study will be achieved under laboratory air at high temperature representative of in-service condition. Guidelines for fatigue crack growth rate modeling in large scale yielding condition is the goal of this study, aiming to assess the role of stress and strain gradient in the choice of the characteristic length of analysis (in a scope of structural analysis, i.e. limiting the mesh size dependency) and associated modeling parameters (i.e. adressing the modeling parameters evolution as a function of the chosen characteristic length of analysis). Thus, typical crack growth specimens (here single edge notched SENT) will be used to identify mechanisms leading to crack growth and model FCGR. To validate this modeling, original specimens comprising multiple holes are used to induce complex interaction between crack and strain localization path.

2. Experimental analysis

The experimental analysis was performed into two ways: a first test series was achieved using SENT specimens in order to analyse crack growth, and identify subsequent crack growth model parameters. This first test series constitutes the aim of this paper. A second test series was achieved to validate the modeling methodology using a multiple holes specimen, that can be seen as a simple structure, details about this test series will be found elsewhere [63, 64, 65].

2.1. Material and specimens

The material used in this study is the Haynes 188 Co based superalloy designed for components operating at high temperature. Its composition is detailed in table 1. All specimens were processed from round bar, obtained after hot rolling following AMS 5878B standard, with an annealing treatment performed from 1177°C to 1246°C during 20 min leading to an average grain size of 90 μm.

Table 1: Chemical composition of Ha 188 superalloy used in the present study (wt %)

Element	Co	Cr	Ni	W	C	La	Si	Fe	Mn
Weight %	Base	22.75	21.85	14.80	0.071	0.08	0.33	2.31	0.94

Single edge notch tension (SENT) specimens were obtained by conventional machining, see Fig. 1, and by wire cut Electro Discharge Machining (EDM) to obtain the notch geometry of 0.2 mm in diameter and of 0.9 mm length including the notch radius, see a_0 in Fig. 2(a). The dimension of the SENT specimens were derived from AFNOR and ASTM standards [66, 67]. The SENT specimen geometry has been introduced to investigate the growth of short cracks under small scale yielding conditions [68, 69] as well as for large scale yielding conditions [54]. In the long crack regime fatigue crack growth results from this SENT geometry were found to be consistent with curves obtained from CT specimens [68, 69, 70]. The three holes specimens are also obtained by classical machining, with the same global geometry excepting the edge notch replaced by holes of 1 mm in diameter, centered in the specimen and which centers are 3 mm spaced, see Fig. 2(b). The chosen geometry was obtained to insure that strain localization paths associated to the holes interact from hole to hole. The details of design were reported in [63, 64]. Holes were processed by die sink EDM. The surfaces of the specimen were polished before testing down to alumina particle size of 1 μm.

2.2. Testing conditions

All tests were strain-controlled. Strain was prescribed using high temperature alumina rod extensometer with a gage length of 10 mm. For SENT specimens, the extensometer was mounted at the

opposite side of the notch. For 3-holes specimens, the extensometer was mounted around the central hole on a face of the specimen.

Crack growth was continuously measured using potential drop technique calibrated on optical measurement performed in situ for SENT specimens, according to [67], and at regular stop for 3-holes specimens. Two probes were welded apart from the notch for SENT specimens and apart from the central hole for 3-holes specimens. For SENT specimens, the crack length measurement a is here assumed to be the sum of the length of the notch and of the physical crack, see Fig. 2(a). For 3-holes specimens, the crack length measurement a is limited to the central hole and here assumed to be the average of the hole diameter and of the physical crack length from both sides of the specimen (back/front) and both sides of the hole (left/right), see Fig. 2(b). For both kind of specimens, the crack length measurement corresponds to the projected length on the direction orthogonal to the loading one. The crack growth rate was obtained using the ratio between a crack length increment $\Delta a = 50$ μm and the corresponding number of cycles increment ΔN.

LCF crack growth tests were performed isothermally at 900°C under laboratory air and for load ratios $R_\varepsilon = 0$ and $R_\varepsilon = -1$. No pre-crack was performed before cycling, since initiation is observed to be very fast under high strain levels as used in this study. Tests conditions are given in table 2. A radiative furnace made of four lamps was used to prescribe temperature which was controlled by S-type thermocouple welded on the specimen gage length [71].

During testing CCD camera was used to monitor crack growth. This was performed using a Keyence VHX1000 with camera size of 1024x1398, with an acquisition frequency of 1 image/cycle. To limit both the temperature of the lens and of the CCD camera and the hot air flux through the furnace window, a piece of quartz has been mounted in front of the furnace window. After testing, the surface of the specimens was observed using optical microscopy (OM) and scanning electron microscopy (SEM). Then specimens were partially cut, using a cutting disk on the remaining ligament, and submitted to monotonous tensile loading up to complete failure of the specimen. The fractured surfaces were observed using OM, SEM and 3D measurement of the surface roughness based on optical microscopy. Digital Image Correlation (DIC) results were obtained using Correli-LMT software [72]. Due to high temperature, surface oxidation provide natural surface patterning. Therefore, no special surface preparation was needed to obtain good DIC results. This "natural" configuration has been already successfully tested for instance in [73, 62] to measure surface displacement field for high temperature coatings.

Table 2: Sent and 3-holes test series conditions, number of cycles to reach a crack length of 5 mm for SENT specimen, N_{max}, or number of cycles to reach a crack length of 900 μm for 3-holes specimen, N_f; all tests were performed at 900°C under laboratory atmosphere

Specimen	$\Delta\varepsilon/2$(%)	Test frequency (Hz)	R_ε	N_{max} or N_f
SENT	0.0625	0.1	0	4106
	0.125			510
	0.25			244
	0.375			168
	0.45			124
3-holes	0.075	0.5	0	38850
	0.1	0.5		21220
	0.15	0.5		1920
	0.25	0.1		177
	0.375	0.1		140
	0.75	0.1	-1	60

3. Experimental results

3.1. Mechanical loading

The chosen testing conditions have led to a wide range of macroscopic loading as highlighted in figure 3, for both SENT and three holes specimens. Lowest applied strain condition, $\Delta\varepsilon/2$ =0.0625 and 0.075% for R_ε=0, are close to macroscopic elastic behavior whereas larger strain conditions exhibit clearly macroscopic plasticity (for $\Delta\varepsilon/2 \geq$0.25%). It is worth noting that for largest applied strain, the material induces stress drop associated to dynamic strain aging. This effect was already observed in [44, 45] at intermediate temperatures of 400°C for $\dot{\varepsilon} = 10^{-4}$. Nevertheless, this behavior was observed in our test series as soon as prescribed strain was greater than $\Delta\varepsilon/2$=0.25%, that could lead locally to high strain rate level. This effect was not observed with 3-holes test series.

3.2. Crack growth

For SENT specimen test series, the maximum test duration exceeds 4.10^3 cycles and was reached for $\Delta\varepsilon/2 = 0.0625\%$ and $R_\varepsilon = 0$. For all others test conditions, tests durations were below few hundreds of cycles. Crack growth initiates mostly below 50 cycles. Associated fatigue crack growth rates (FCGR) are very high and range from 10^{-6} m/cycle up to 10^{-4} m/cycle. The FCGR for $\Delta\varepsilon/2 = 0.0625\%$ / $R_\varepsilon = 0$ is consistently much lower than other conditions: for this test condition, macroscopic behavior is seen to be elastic whereas macroscopic plasticity is observed for the whole test series with higher applied strain.

For 3-holes specimen test series, the range of test duration is consistent with results obtained for SENT test series considering large strain values and significatively longer for low strain loading levels, Table 2. Initiation was detected only during optical inspection and could have occurred before the stop, considering three-dimensional effects associated to the hole geometry and the ratio between hole diameter and specimen thickness.

3.3. Crack path and surface observations

SENT specimen. Crack growth starts with a planar crack morphology, mostly orthogonal to the loading direction, Fig. 5. For lowest strain condition, and subsequent small scale yielding condition, the crack path stays straight during the whole test, with neither significant crack deviation nor evidence of significant damage in the vicinity of the crack path and around the crack tip, Fig. 5(a). Increasing the applied strain level, a flat to slant crack path appears, Fig. 5(b) and (c). The higher the strain level, the smaller horizontal crack path is observed, Fig. 5. For medium to high strain level, multiple cracks initiate on the notch, but only one of them will drive to the major crack that is considered for crack length measurement. Crack tip blunting is in these cases observed for the major crack. The large scale yielding is directly observed on the surface of the specimen where large modifications of the surface roughness is observed according to both the crack path and the crack wake, Fig. 5. Indeed, contrast modification of the surface of the specimen is due to significant oxide spallation associated to the highest strained areas, Fig. 5. Moreover, damage is evidenced for long cracks where micro-cracks appear on the surface, see in situ optical images corresponding to the maximum loading during cycling in Fig. 5(b) and (c).

The use of DIC enables to evidence strain field localization associated to the notch specimen at the beginning of the test, Fig. 6, prior to significant crack growth. Maximum strain values exceeds here 1% for an averaged maximum applied strain of 0.5%. Strain values exceeding 0.5% are found in a radius of 2.5 mm from the notch. This very large area of high strained material is fully consistent with measurement based on twinning density and micro-hardness for a Co-Ni alloy tested at room temperature [74]. Moreover, the strain localization pattern appears not to be symmetric according to the mid plane of the specimen. Thus, in this area, strain values exceeding 0.8% are found in a radius of 3 mm from the notch. This loss of symmetry is consistent with the observed crack path, Fig. 5(b), indicated by a black arrow in Fig. 6: two cracks have been initiated on the notch, but only one of them will drive to the major crack. In situ images have enabled to perform high resolution strain field measurement taking into consideration the temperature of 900°C. Nevertheless, only relatively low applied strain and short crack could be analyzed; otherwise, micro-cracks would lead to erroneous assessment of strain values.

Detailed observations can be made during crack growth from in situ images corresponding to maximum applied strain, Fig. 7. Micro-cracks are observed within strain localization path and ahead of the major crack or secondary cracks. For exemple, the micro-crack arrowed in Fig. 7(a) (red arrow) is more than 300 μm ahead of one of the secondary crack linked to strain localization path and coalesces in approximatively 10 cycles with this secondary crack. The micro-crack arrowed in Fig. 7(b) (white arrow) is less than 250 μm ahead of the major crack and coalesces in less than 5 cycles with the major crack. For secondary cracks, micro-cracks seem to grow substantially before the coalescence. Whereas,

for the major crack, these surface observations show that the major crack growth is much more faster than the micro-crack growth. These observations made for these two micro-cracks could be generalized for other micro-cracks on this set of pictures and for other testing conditions as soon as significant plasticity is observed (i.e. for large applied strain values or for long crack). Micro-cracks lengths range from 10 μm up to 200 μm for the highest tested levels. For high strain loading condition, as typically observed in Fig. 5(c), the major crack path is close to the initial strain localization path in one direction after branching. Thus the growth of micro-cracks pattern, before the coalescence with the major crack, could be observed. Nevertheless, the fatigue crack growth rate becomes very high for these loading conditions and micro-cracks growth and coalescence with the major crack fall in the same cycle and will not be more detailed in the sequel.

After test completion, SEM surface observations have enabled to confirm that for initiation, Fig. 8(b), and during crack growth, Fig.8(c), many local crack bifurcations occur, Fig. 8. A zoom in the final crack tip region using back scattered electron (BSE) mode also highlights that both crack and micro-cracks are certainly inter-granular, Fig. 8(d). These observations substantiate that the principal crack grows in a pattern of micro-cracks and that the process zone size is quite large for these LCF loading conditions.

Fractured surfaces observations bear out that a flat to slant crack arises for large applied strain values. The flat part of the crack corresponds to few mm crack growth, for instance around 1 mm for $\Delta\varepsilon/2 = 0.45\%$, $R_\varepsilon = 0$, Fig. 9. Considering the slanted part of the crack e.g. for a crack length of about 5 mm, the height difference between front and backside of the specimen is of about 2.5 mm, Fig. 9(b). Moreover, steps have appeared in the last part of the slanted region, that could be linked to a mode I to a mode I+III transition inducing typical roof shape of fracture [75, 76], label 3 Fig. 9. This point is out of the scope of this paper and will not be detailed next.

Finally, observation of fracture surface could locally suggest intergranular crack growth for $\Delta\varepsilon/2 = 0.25$ and $R_\varepsilon = 0$ test, Fig. 10(a). Nevertheless, for test with higher strain range, compression loading deforms fatigue fracture surfaces and prevents their analysis, $\Delta\varepsilon/2 = 0.45$ and $R_\varepsilon = 0$ test, Fig. 10(b).

Three holes specimen. The same global behavior of cracks as function of the applied strain level is observed for 3-holes specimens as compared to SENT specimens: based on surface observation, cracks are initially flat and deviate from path orthogonal to the loading direction for tests with significant macroscopic plasticity (typically for $\Delta\varepsilon/2 \geq 0.25\%$). For smaller applied strain values, crack paths remain mostly flat, Fig. 11(a). Deviation is increased with increasing length and increasing applied strain level. Evidences of strain localization are found to be linked with a significant increase of the surface roughness, see lateral hole on the right side of Fig. 11(b). The observed contrast in Fig. 11(b), corresponds at a very local scale to oxide ridges, that could be associated to grain boundaries or slip plane, Fig. 11(c) and (d). As detailed for SENT specimens, micro-cracks are observed to take place

around the crack tip and within the crack wake for large applied strain level, Fig. 11(b) and (d). Again, multiple cracks initiate on holes (in most cases three cracks are observed on each side of the central hole using in situ observation not shown here) but only one of these micro-cracks will lead to the major crack, Fig. 11(b). Nevertheless, the huge difference between SENT and 3-holes specimens is the interaction of cracks emanating from different holes. For low applied strain level, interaction of cracks from central and lateral holes is not clear since the crack path remains mostly straight during its growth, Fig. 11(a). On the other hand, for larger applied strain values, multiple crack deviations are observed along the major crack path until crack coalescence between cracks emanating respectively from the central and the lateral holes, Fig. 11(b). As observed for SENT specimen, crack closure induced by large scale yielding conditions prevents the analysis of fractured surface. For 3-holes specimen, for large strain ranges, stress-strain loops suggest that compliance changes at negative loads, Fig. 3(b). But no attempt was made to account for crack closure in the analysis of the results. In the sequel, only SENT specimens will be detailed since fatigue crack growth mechanisms are comparable for both 3-holes and SENT specimens before interaction of cracks initiated on two holes.

4. Modeling fatigue crack growth under large scale yielding condition

4.1. Macroscopic model

The chosen model was previously developed for a macroscopic analysis of crack growth under isothermal LCF tests performed on notched hollow specimens [28]. The main idea of this model is to partition the driving force of crack growth into elasticity, relative to hydrostatic part of the stress tensor, and plasticity, related to shear and deviatoric part of the stress tensor using a strain energy analysis. The original model of crack growth was as follow:

$$\frac{1}{\lambda}\frac{da}{dN} = \left(\beta_e \frac{W_e}{\gamma_e} a\right)^{m_e} + \left(\beta_p \frac{W_p}{\gamma_p} a\right)^{m_p} \tag{1}$$

where γ_e, γ_p, m_e, m_p and λ are the model parameters. The parameters β_e and β_p should be seen as geometrical parameters. The terms W_e and W_p are associated to elastic opening energy and plastic distortion energy respectively following the set of equations:

$$W_e = \frac{1}{3}\int_{cycle} < tr(\underset{\sim}{\boldsymbol{\sigma}}) > . < tr(d\underset{\sim}{\boldsymbol{\varepsilon}}^e) > \tag{2}$$

$$W_p = \int_{cycle} \underset{\sim}{\boldsymbol{s}} : d\underset{\sim}{\boldsymbol{\varepsilon}}^p \tag{3}$$

where $\underset{\sim}{\boldsymbol{\sigma}}$, $\underset{\sim}{\boldsymbol{\varepsilon}}^e$ and $\underset{\sim}{\boldsymbol{\varepsilon}}^p$ correspond respectively to stress, elastic strain and plastic strain tensor, tr is the first invariant of the considered tensor, and <.> corresponds to the Macaulay brackets, e.g. $< tr(\underset{\sim}{\boldsymbol{\sigma}}) >= tr(\underset{\sim}{\boldsymbol{\sigma}})$

if $tr(\underset{\sim}{\boldsymbol{\sigma}}) > 0$ and $< tr(\underset{\sim}{\boldsymbol{\sigma}}) >= 0$ otherwise. These energy terms were deduced from stress-strain values yielded by force and extensometer strain measurement, values that can be obtained either from direct experimental results or from FE analysis of the tested specimen (e.g. SENT, notched hollow specimen...) [28]. Thus the model was originally designed to take into consideration geometry of the specimen through the parameters β_e and β_p to analyze other specimen geometries. The idea was to modify the effect of singularity in the same way as usually performed with shape function in linear elastic fracture mechanic. This was successfully achieved using known solutions for penny-shape like defects and has enabled to use the same model parameters to obtain life of smooth specimens. Nevertheless, this method is not general enough to encompass the broad range of geometry observed in most of applications except if tabulation of shape parameters are performed before. Thus, the following post-processing approach is a simple way to overcome this drawback.

4.2. Post processing analysis

The post-processing method is built to estimate crack growth rate, and subsequent number of cycles leading to a given crack growth, on a user defined set of elements. The growth rate model is taken in the form:

$$\frac{1}{\lambda}\frac{da}{dN} = \left(\frac{w_e}{\gamma_e}a\right)^{m_e} + \left(\frac{w_p}{\gamma_p}a\right)^{m_p} \tag{4}$$

which is the same model as presented in equation 1 setting the geometrical parameters β_e and β_p to unity. The post-processing approach is in fact a direct way to take into consideration geometry influence on local mechanical loading through the numerical computation of energy terms w_e and w_p averaged on the volume to be analyzed $\Omega = \sum_{i=1}^{n} d\Omega_i$ as:

$$w_e^* = \frac{1}{\Omega}\sum_{i=1}^{n} W_e d\Omega_i \tag{5}$$

$$w_p^* = \frac{1}{\Omega}\sum_{i=1}^{n} W_p d\Omega_i \tag{6}$$

where W_e and W_p correspond respectively to equations 2 and 3 which are determined locally for each of the n integration points within the volume Ω.

Finally, the crack growth rate equation is integrated using a Runge-Kutta method for an a priori high number of cycles exceeding LCF range (e.g. 10^8 cycles). The number of cycles to failure is the result of this integration for the chosen failure crack length a_f:

$$N_f = \int_{a_0}^{a_f} \frac{da}{\frac{da}{dN}(W_e, W_p; a)} \tag{7}$$

The above equations have been implemented in the Zset code, in an oriented object langage close to c++ [77, 78, 79]. The algorithm could be summarized as follows:

1. **choice of a given loading cycle**; this choice is user defined since it will be strongly dependent on the used mechanical behavior model, as a general guide at least two cycles should be computed to take into consideration stress redistribution after first monotonic loading. This point is widely debated through fatigue analysis but here should not be analyzed as a "stabilized cycle", i.e. for a typical Chaboche law using kinematic and isotropic hardening, the sensitivity was rather low to this chosen cycle [28].
2. **choice of a volume ahead of the crack tip or notch or any mechanical singularity to be studied**; this choice is user defined and will greatly impact the subsequent analysis. As it would be detailed in the sequel, the characteristic length of the chosen volume should be seen as a mechanical parameter of the fatigue crack growth rate analysis. The way this volume should be chosen will be defined later on in the paper, taking into consideration sensitivity analysis.
3. **computation of opening elastic energy W_e and plastic distortion energy W_p**; these quantities are determined locally for each of the n integration points.
4. **averaging of elastic and plastic energies over the chosen volume**; according to eqs. 5 and 6
5. **computation of crack growth rate**; according to eq. 4

This scheme corresponds to the set of equations 4 to 6 and leads to

$$da/dN = f\left[w_e^*(\underset{\sim}{\boldsymbol{\sigma}}, \underset{\sim}{\boldsymbol{\varepsilon}}_e), w_p^*(\underset{\sim}{\boldsymbol{s}}, \underset{\sim}{\boldsymbol{\varepsilon}}_p); a\right]$$

which equation yields to the fatigue crack growth rate on the chosen volume of integration. Two more points should be added to obtain a failure criterion, namely:

6. **integration of crack growth rate** ; it consists in resolving a non linear differential equation $da/dN = f(a)$ to determine the crack length as a function of the number of cycles, namely $a(N)$
7. **determination of N_f**; according to eq. 7

4.3. 3D modeling of the testing configuration

The aim of this numerical study besides in the identification of crack growth model based on mechanical stress, strain and subsequent energies in the geometrical configuration before crack initiation. Thus, for reason of symmetry, only a quarter of the specimen is modeled for both SENT and 3-holes specimens using quadratic reduced elements, Fig. 12. Boundary conditions are used to simulate mid-plane symmetry (xy) orthogonally to the loading direction, where U_y is set to zero, Fig. 12(a) and (c), and mid-plane

symmetry (xz) parallel to the loading direction and the free surface of the specimen, where U_z is set to zero, Fig. 12(b). The surface $z = 2$ corresponds to the free surface of the specimen where cracks and surface strain are optically measured. Tests are controlled by homogeneous prescribed displacement of the top surface of the specimen. Thus, a control point corresponding to the extensometer contact point is used to check the experimental prescribed deformation on the basis of extensometer gage length. The same methodology is applied for 3-holes specimens, using an additional symmetry condition along the (yz) plane where U_x is set to zero, Fig. 12(c).

The mechanical behavior is described through a two potentials Chaboche model, see Table 3, detailed in [80, 81, 82] that was seen to reproduce merely the behavior of the considered material out of the Dynamic Strain Aging domain [83].

Table 3: "Two potentials" behavior used for Ha188 ; kinematic and isotropic hardening are considered for a "quick" and a "slow" term accounting for strain rate influence

Strain partitioning	$\underset{\sim}{\varepsilon}^{tot} = \underset{\sim}{\varepsilon}^{e} + \underset{\sim}{\varepsilon}^{p}$
Yield function	$f = \sqrt{\frac{3}{2}(\underset{\sim}{s} - \underset{\sim}{X}) : (\underset{\sim}{s} - \underset{\sim}{X})} - \sigma_y - R$
Kinematic Hardening	$\dot{\underset{\sim}{\alpha}} = \dot{\underset{\sim}{\varepsilon}}^{p} - \gamma \underset{\sim}{\alpha} \dot{p}$
	$\dot{\underset{\sim}{X}} = \frac{2}{3} C \dot{\underset{\sim}{\alpha}}$
Isotropic Hardening	$R = R_\infty (1 - e^{-bp})$
Flow Function	"quick" term $\dot{p}_q = \left\langle \frac{f}{K_N^q} \right\rangle^{N^q}$
	"slow" term $\dot{p}_s \left\langle \frac{f}{K_N^s} \right\rangle^{N^s}$
Total cumulated plasticity	$\dot{p} = \dot{p}_q + \dot{p}_s$

The stress and strain fields show that 3D effects influence strongly local stress and strain distribution, Fig. 13. The maximum out-of-plane stress is reached in the mid-plane section beyond the notch root, Fig. 13(a), whereas maximum of strain is located at sub-surface, Fig. 13(b). Due to large local strain values, it is useful to analyze the role of hydrostatic pressure, namely σ_H, using the stress triaxiality ratio defined as σ_H/σ_{eq} where σ_{eq} corresponds to the von Mises criterion. The observed maximum stress is consistent with the locus of maximum stress triaxiality ratio, Fig. 13(a) and (c).

These trends are confirmed by analyzing stress and inelastic strain evolutions along mid-plane and surface plane of the specimen: stress values are not monotonic as a function of the distance from the notch root, Fig 14(a), and reach their maximum values at 100-200 μm from the notch root. Inelastic strain values decrease monotonically at maximum applied strain, Fig. 14(b). The evolution of stress is connected to the location of stress triaxiality ratio peak value, that depends on depth of analysis from

the surface plane: it is located at approximatively 200 μm from the notch root at the mid-plane and below 100 μm for the external free surface, for an applied loading of $\Delta\varepsilon/2 = 0.375\%$, Fig. 14(c). For smaller applied loading, the level of triaxiality decreases but its location is close to what was observed for maximum applied loading for both mid-plane and external free surface of the specimen.

Since chosen crack growth modeling is based on elastic and plastic energies defined in eqs. 2, these quantities should be locally analyzed. Plastic energy decreases monotonically from the notch root, Fig. 15. It is worth noting that at the notch root, maximum of plastic energy is found at the mid-plane of the specimen, whereas for a distance from the notch root above 100 μm, the plastic energy is maximum at the subsurface, Fig. 15(a). Besides, the location of the maximum of elastic energy, for high level of strain loading, is found to vary from 50 to 100 μm from external surface to the mid-plane of the specimen, Fig. 15(a). This is consistent with results obtained for maximum of triaxiality stress ratio since elastic energy is based on hydrostatic pressure (see eq. 2). For lower applied strain values, similar spatial evolutions of energy are observed, excepting that elastic and plastic energies values can be very close to each other, or even elastic energy can exceed plastic one, Fig. 15(b). For surface values, maximum of elastic energy is located at the same distance from the notch root close to $r = 50$ μm, irrespectively to the tested applied strain value. Basically, same trends are found for 3-holes specimen considering location of maximum stress triaxiality ratio and other mechanical quantities detailed for SENT specimens and thus will not be detailed in the sequel.

On the basis of the stress, strain, triaxiality and energy gradients analysis, it is clearly expected that, with the chosen notch geometry, the choice of a box size will greatly impact the evaluation of averaged plastic and elastic energy values. Moreover, it appears that below 100-200 μm from the notch root, stress or inelastic strain values are not monotonic as a function of the distance from the notch root. Thus it could be straightforward to take into consideration box for averaging values larger than this distance that appears as a transition length.

4.4. Sensitivity analysis of energy computation

A sensitivity analysis was achieved on the basis of loading parameters corresponding to SENT specimen test series. The range of applied strain is broad enough to go from small to large scale yielding conditions. The average analysis of mechanical quantities is achieved for 3D mesh presented above and for cubic boxes, see highlighted areas in Fig. 12. For reason of symmetry, since only a quarter of the specimen is modeled, only half of "cubic" boxes are shown. To increase the reliability of local crack length measurement and proposed modeling of crack growth, only near surface boxes are considered in this analysis. That is to say that energy is averaged in boxes with one face corresponding to the specimen surface and one face tangent to the notch root. This point is very close to non-local analysis here used for a simplified non-local function similar to a low pass filter. On the basis of above results concerning

the low sensitivity of energy assessment to the number of cycles for both specimen [28] and structure [84], only 10 cycles have been computed for each case detailed below.

Influence of the mesh size. To estimate the influence of the mesh size on energy values assessment, the mesh size in the vicinity of the notch was varied from 5 to 125 μm. The box size was set to 250 μm and energy values were estimated for $\Delta\varepsilon/2$ ranging from 0.0625 to 0.375%, see Table 4 for results.

Table 4: Influence of the mesh size on plastic and elastic energies values. The ratios $w_p^*/w_p^*(h = 125\,\mu m)$ and $w_e^*/w_e^*(h = 125\,\mu m)$ correspond respectively to the ratios of the computed plastic and elastic energies obtained for the chosen mesh size h and energies obtained for a mesh size of 125 μm. These ratios are tested for each strain levels

$\Delta\varepsilon/2(\%)$	mesh size h (μm)	w_p^* (J/m^3)	w_e^* (J/m^3)	$w_p^*/w_p^*(h = 125\,\mu m)$	$w_e^*/w_e^*(h = 125\,\mu m)$
0.0625	125	$8.94.10^5$	$2.56.10^5$	1	1
	50	$8.96.10^5$	$2.57.10^5$	1.002	1.005
	25	$8.95.10^5$	$2.57.10^5$	1.001	1.005
	10	$8.95.10^5$	$2.57.10^5$	1.001	1.005
	5	$8.94.10^5$	$2.57.10^5$	1	1.004
0.125	125	$6.38.10^6$	$6.62.10^5$	1	1
	50	$6.28.10^6$	$6.66.10^5$	0.984	1.006
	25	$6.27.10^6$	$6.65.10^5$	0.983	1.005
	10	$6.17.10^6$	$6.65.10^5$	0.983	1.005
	5	$6.17.10^6$	$6.66.10^5$	0.985	1.006
0.250	125	$2.55.10^7$	$9.79.10^5$	1	1
	50	$2.50.10^7$	$9.79.10^5$	0.979	1
	25	$2.50.10^7$	$9.78.10^5$	0.978	0.999
	10	$2.49.10^7$	$9.78.10^5$	0.977	0.999
	5	$2.49.10^7$	$9.78.10^5$	0.975	0.999
0.375	125	$5.04.10^7$	$1.16.10^6$	1	1
	50	$4.92.10^7$	$1.16.10^6$	0.977	0.998
	25	$4.91.10^7$	$1.16.10^6$	0.976	0.997
	10	$4.91.10^7$	$1.16.10^6$	0.976	0.997
	5	$4.91.10^7$	$1.16.10^6$	0.975	0.997

Tested conditions lead to energy variations less than 2.5%. Thus, in the following, the minimum mesh size is set to 50 μm for which values, the energy assessment could be claimed to be independent of the mesh size.

Influence of the box size. This analysis is performed for a minimum mesh size, set to a value of 50 μm as discussed above. The resulting elastic and plastic energies are plot as a function of the box length, l_c, and of the applied strain values corresponding to SENT test series. The range of elastic energy spreads from 4.10^4 to 10^6 J.m^{-3} with a clear asymptotical value found for large applied strain values, Fig. 16(a). The elastic energy found for the 125 μm box size is more than 7 times the elastic energy found for the 4 mm box size. The range of plastic energy spreads from 6.10^4 to 10^8 J.m^{-3} with a higher sensitivity to large

applied strain values than for elastic energy, Fig. 16(b). The plastic energy found for the 125 μm box size could be more than 30 times the plastic energy found for the 4 mm box size. It is also shown that for both tests drove at $\Delta\varepsilon/2 = 0.0625\%$ and $\Delta\varepsilon/2 = 0.125\%$ elastic and plastic energy values are of the same order of magnitude, whereas for larger applied strain values plastic energy exceeds clearly elastic energy for any box size. This point implies that test series could be ranked into tests where competition between elasticity and plasticity would influence crack growth rate and others where plasticity (or to a less extent elasticity) will only governs crack growth rate. As a partial conclusion, averaged energy values are strongly dependent of the box size, but the evolution of the ratio of energy from high to low applied strain is relatively independent of the box size. This point is of interest for the robustness of crack growth model identification as it will be discussed later on.

5. Results of crack growth model applied as a post-processor

This section is devoted to crack growth model identification and validation. Identification was performed on the basis of crack growth rate observed experimentally for SENT specimen test series. It has been shown above that the mesh size dependency was rather low averaging strain energy in a given volume described as a cubic box, but that the choice of the characteristic length describing the box size drastically impacts the obtained energy values. Thus, the aim of this part is to analyse what is the range of application of the chosen FCGR model and how to take into consideration the choice of this characteristic length on the quality of FCGR modeling. A final validation was performed on the basis of the number of cycles leading to a given crack length for the 3-holes specimens test series without modification of previous set of crack growth model parameters.

5.1. Model identification

To estimate the influence of the box size used for energy averaging, the procedure of crack growth model parameters identification was applied for box sizes varying from 125 μm to 4 mm. The fatigue crack growth model refers to equations 2 to 6. As discussed in [28], the λ parameter should exceed the average grain size of the considered material, and is here set to $\lambda = 140$ μm. This parameter is of a low sensitivity on model identification, since it only impacts the obtained values of surface energies γ_e and γ_p without influence on the γ_e/γ_p ratio and subsequent crack growth rate. Firstly, both elastic crack growth rate exponent m_e and plastic crack growth rate exponent m_p are identified on the basis of the lowest and tested strain values respectively, i.e. for $\Delta\varepsilon/2 = 0.0625\%$, $R_\varepsilon = 0$, test and $\Delta\varepsilon/2 = 0.45\%$, $R_\varepsilon = 0$, test. This procedure leads to optimal values of $m_e = 1.5$ and $m_p = 2$. For sake of clarity, only γ_e and γ_p will be varied as a function of the box size while keeping exponents m_e and m_p and λ model parameter at constant values. Thus, secondly, γ_e and γ_p are optimized through minimisation of a cost function

based on least square method between experimental and modeled fatigue crack growth rate [28]. This last step is performed sequentially on the lowest applied strain value test condition, to find the optimal γ_e value and then on the whole database to find the optimal γ_p value. The modeled crack growth rate are compared to experimental values for each box size, Fig. 17.

The optimization procedure has led to a very good correlation between modeled and experimental crack growth rate for high applied strain levels, see Fig. 17. It is worth noting that, when increasing the box size above 1 mm, the quality of optimization decreases for high strain levels, because of the choice made of optimizing only γ_e and γ_p values. Thus, the quality of the identification could be enhanced modifying m_e and m_p but would limit the clarity of the proposed sensitivity analysis. Moreover, the chosen model and optimization procedure has led to a fatigue crack growth rate above the experimental one for the lowest applied strain value test condition, i.e. for $\Delta\varepsilon/2 = 0.0625\%$, $R_\varepsilon = 0$, test for box sizes of 125 and 250 μm. Nevertheless, the model has shown its ability to encompass a broad range of applied strain values for a large variation of chosen box size.

The evolution of γ_e and γ_p parameters decrease monotonically as a function of the chosen box size l_c, for $l_c \geq 250\mu$m, Fig. 18. For $l_c = 125$ μm, the γ_e value is smaller than the optimized value found for $l_c = 250$ μm. These effects are related to the evolution of energies as a function of the box size, Fig. 15. It is now possible to assume that the model could be seen in a more general way as:

$$\frac{1}{\lambda}\frac{da}{dN} = \left(\frac{w_e^*}{\gamma_e(l_c)}a\right)^{m_e} + \left(\frac{w_p^*}{\gamma_p(l_c)}a\right)^{m_p} \tag{8}$$

where l_c is the characteristic length of the box size used for averaging energy values.

$$\frac{1}{\lambda}\frac{da}{dN} = \left(\frac{w_e(a)^*}{w_e^*(l_c)}\right)^{m_e} + \left(\frac{w_p(a)}{w_p^*(l_c)}\right)^{m_p} \tag{9}$$

5.2. Validation

Based on the above identification of crack growth model parameters, the 3-holes specimen test series is used to validate the crack growth model. The same procedure of averaging elastic and plastic energy values is processed taking into consideration the central hole where cracks were measured. For sake of consistency with identification procedure, cubic boxes used for averaging had one face located on the specimen surface and one face tangent with the hole, Fig. 12. These averaged energies have enabled to estimate the crack growth rate and the number of cycles N_f required for the crack to reach a final crack length a_f, as detailed in eq. 7. This integration step has been performed from an initial crack length $a_0 = 590$ μm up to a final crack length $a_f = 900$ μm, taking into consideration the hole radius of 500 μm. The initial crack length corresponds to the measured average grain size of the material, and was also observed to be close to the typical micro-crack length at initiation observed for 3-holes specimen [63, 64].

The relatively low crack extent was straightforward to avoid crack length for which large deviations of crack path was systematically observed and for which the interaction of cracks emanating from each hole was experimentally observed. Indeed, since no explicit crack growth is modeled through FEA, this interaction could not be taken into consideration in this study. The direct comparison between measured and modeled number of cycles N_f to reach a final crack length $a_f = 900$ μm was obtained for box size varied from 125 μm to 1 mm, Fig. 19.

Obtained results show a very good correlation between experimental and modeled life assessment: the results deviate at the maximum of a factor of three irrespectively of the characteristic length varied from 125 μm to 1 mm.

6. Discussion

For the high temperature conditions tested in this study, a clear transition has been evidenced between small and large scale yielding condition. Firstly, increasing the applied strain level, a high increase in FCGR has been observed together with a large hysteresis in macroscopic stress-strain evolution. Secondly, the crack path goes from flat to slant. In the same time, the material ahead of the major crack is seen as a smooth surface with no evidence of defect for low applied strain values, whereas, the major crack grows in a complex pattern of micro-cracks for high applied strain values or long crack. These micro-cracks are typical of inter-granular failure observed in creep conditions [10] or oxidation assisted creep [55] and are certainly induced by high temperature and high local stress levels. The micro-cracks were observed on specimen free surface for high applied loading, Fig. 5, 7 and 8, as well as on fractography observation, Fig. 10(a). This evolution of fatigue crack growth and damage mechanisms have been observed to be fully consistent for both SENT and 3-holes specimens. About interaction between major crack path, micro-crack pattern and strain localization path, differences have been evidenced between the two set of specimens and short crack versus long crack behavior. For relatively long crack in SENT specimens, the micro-cracks associated to strain localization and secondary cracks open when they are located ahead of the major crack tip (see Fig. 7(a)) and close when they are located in the wake of the major crack (see Fig. 7(i)). Finally, the secondary crack patterns orientation and localization have little influence on the major crack path. This kind of crack path evolution, associated for long crack to a flat to slant fracture transition has been widely commented in monotonic ductile failure and is associated to a global energy minimization process [85, 86]. On the other hand for highest loading, for relatively long cracks considering 3-holes specimens as well as for short crack considering both SENT and 3-holes specimens, the major crack path is clearly associated to strain localization path, Fig. 5(c) and Fig. 11(b) respectively. That is to say that, the 3-holes specimen geometry finally leads to a large interaction between plasticity induced by the crack tip and by the holes.

Again, for monotonic ductile failure, it has been well established that the occurence of failure beyond the crack tip is strongly related to local peak value of stress triaxiality ratio [34]. For fatigue loading under large scale yielding condition, crack tip blunting is clearly observed. Thus the chosen size of the notch radius is relatively close to crack tip radius, making FEA of the initial configuration relevant to discuss mechanical field for crack. Thus, the proposed FEA has shown that the location of peak value of stress triaxiality ratio, Fig. 14(c), and associated peak value of elastic energy, Fig. 15, are consistent with the observed surface micro-cracks, Fig. 7. Even if this observation is limited to surface, it does suggest that stress triaxiality could strongly influence the failure of the considered material: ahead of the major crack tip, micro-cracks initiate at maximum stress triaxiality and because of the high fatigue crack growth rate, the remaining ligament between the major crack tip and the tip of the closest micro-crack could be broken within very few cycles.

For material where brittle particles govern the crack growth rate, for instance for cast aluminium alloys, X-Ray tomography has enabled to obtain 3D observations of interactions between multiple micro-cracks and defects [87], and to highlight the correlation between maximum stress triaxiality ratio and local failure of the material for low cycle fatigue loading [88]. But it remains still challenging on the one hand to perform 3D X-Ray observation of damage for high atomic density materials as used in this study for significative volume of matter, and on the other hand to explicitly model small crack interaction with complex 3D microstructure.

The proposed post-processing methodology has been successfully applied to two different geometries for identification and validation of the model parameters. The fatigue crack growth model is a function of averaged elastic and plastic energies. The averaging is achieved in a given volume designed as a simple box [1]. This average step is indeed a simple non-local approach for which the choice of the characteristic length impacts directly the values of the crack growth model parameters. As a general guideline, it appears that the characteristic length for averaging energy should be larger or equal to the typical distance between the notch root and the locus of the peak of stress triaxiality. For the analyzed test series, optimized characteristic length are of $250\ \mu m \leq l_c \leq 1\ mm$ for SENT test series and increases to $500\ \mu m \leq l_c \leq 1\ mm$ for 3-holes test series. This effect is consistent with notch radius respectively of 100 and 500 μm for SENT and 3-holes specimens. This approach is moreover very convenient to limit the influence of mesh size and limit the computation cost for structure application. Finally, this quite large characteristic length should be seen as a process zone which size is consistent with observed micro-cracks pattern induced by large scale yielding, the size of this pattern being observed to be very large as compared to the average grain size since it is mostly driven by the strain localization.

At last but not least, the integration of the crack growth rate model is also effective to obtain life

[1] Varying shape of the box used for energy averaging from cube to sphere of same volume located at the edge of the notch, very little influence was observed on averaged energy values.

assessment of 3-holes specimen seen as a structural case. Let's go back to assumptions made for this modeling and some questions raised by them. At a first point no crack growth have been introduced here. Thus amplification of crack growth rate with crack growth has been modeled using a coupling between crack growth rate and crack length, i.e. $da/dN = f(a)$. The obtained results are reliable for single crack configuration, as usually performed with Paris model for small scale yielding condition, but could not take into consideration large variation of loading observed for exemple when cracks are very long and close to coalesce for 3-holes specimens. Explicit crack growth model by FEA would therefore enable to assess local loading evolution as a function of the crack location and path, and could be developed according to either X-FEM tools [89, 90] or conform remeshing technique as developed in [91]. Moreover, experimentally it has been clearly observed that crack deviation was of a great importance in the tested configuration. This point needs to be carefully analyzed since it will drastically impact the local loading at the crack tip and subsequent evaluation of elastic and plastic energies, and prescribes the analysis of crack mode mixity. The explicit FEA of crack growth can be straightforward to analyze locally this issues taking into consideration a large variety of crack location and morphology.

Conclusion

This paper has shown fatigue crack growth behavior for strain controlled tests performed at 900°C for Haynes188, Co base superalloy. These test series have been carried out from small to large scale yielding conditions. A systematic fatigue crack growth modeling was applied for the tested configurations. Main results could be summarized as follows:

- Fatigue crack growth rate increases with applied strain values. A large increased in FCGR was observed as soon as macroscopic plasticity was measured.
- The crack path shows a typical flat to slant transition for highest strain values for SENT specimens.
- The major crack was revealed to interact with a micro-crack pattern, suggested to be intergranular and correlated to the strain localization path. This strain localization path is associated to the specimen geometry (for either SENT or 3-holes specimens). Moreover, multiple cracking interactions have been observed for 3-holes specimens (cracks emanating from each holes).
- The chosen crack growth rate model, based on energy assessment is effective to model both crack growth rate and to assess life after integration of the crack growth rate, for respectively SENT and 3-holes specimens .
- The model parameters are function of the characteristic length where strain energy values are averaged, making the choice of this characteristic length crucial for part modeling.

Acknowledgements

This work was partially funded by the French Ministry of Transportation (Direction des Programmes de l'Aviation Civile) and the French Ministry of Defence (Délégation Générale à l'Armement) who are acknowledged for, during the program "PRC Structures Chaudes". This work was also funded by the National ANR grant ANR-14-CE07-0037 Semafor, headed by Vincent Chiaruttini (ONERA) who is greatly acknowledged. Vladimir Esin, Mines ParisTech, and Valentin Bourrelier, Antoine Marchal and Dimitri de Plasse students at Mines ParisTech are acknowledged for their kind help in crack imaging.

Bibliography

References

[1] R. Lardner, A dislocation model for fatigue crack growth in metals, Philosophical Magazine 17 (145) (1968) 71–82.

[2] K. Tanaka, T. Mura, A dislocation model for fatigue crack initiation, Journal of Applied Mechanics 48 (1) (1981) 97–103.

[3] C. Laird, The influence of metallurgical structure on the mechanisms of fatigue crack propagation, in: Fatigue crack propagation, ASTM International, 1967.

[4] K. Tanaka, T. Hoshide, N. Sakai, Mechanics of fatigue crack propagation by crack-tip plastic blunting, Engineering Fracture Mechanics 19 (5) (1984) 805–825.

[5] Y. Guilhem, S. Basseville, F. Curtit, J.-M. Stephan, G. Cailletaud, Investigation of the effect of grain clusters on fatigue crack initiation in polycrystals, International Journal of Fatigue 32 (11) (2010) 1748–1763.

[6] F. McClintock, Fatigue crack propagation, ASTM STP 415 (1967) 170.

[7] S. D. Antolovich, A. Saxena, G. R. Chanani, A model for fatigue crack propagation, Engineering fracture mechanics 7 (4) (1975) 649–652.

[8] G. Chalant, L. Remy, Model of fatigue crack propagation by damage accumulation at the crack tip, Engineering Fracture Mechanics 18 (5) (1983) 939–952.

[9] F. Bridier, P. Villechaise, J. Mendez, Slip and fatigue crack formation processes in an α/β titanium alloy in relation to crystallographic texture on different scales, Acta Materialia 56 (15) (2008) 3951–3962.

[10] J. Weiss, A. Pineau, Fatigue and Creep-Fatigue Damage of Austenitic Stainless-Steels Under Multiaxial Loading, Metall. Trans. A 24 (10) (1993) 2247–2261. doi:{10.1007/BF02648599}.

[11] W. Z. Abuzaid, M. D. Sangid, J. D. Carroll, H. Sehitoglu, J. Lambros, Slip transfer and plastic strain accumulation across grain boundaries in hastelloy x, Journal of the Mechanics and Physics of Solids 60 (6) (2012) 1201–1220.

[12] L. Remy, A. Alam, N. Haddar, A. Köster, N. Marchal, Growth of small cracks and prediction of lifetime in high-temperature alloys, Materials Science and Engineering: A, 468-470 (2007) 40–50.

[13] J. Rice, A path independent integral and the approximate analysis of strain concentration by notches and cracks, ASME J. Appl. Mech. E. 35(2) (1968) 379–386.

[14] N. E. Dowling, J. A. Begley, Fatigue crack growth during gross plasticity and the j-integral, Mechanics of Crack Growth.ASTM, Philadelphia, Pa.1976.

[15] K. Tanaka, The cyclic j-integral as a criterion for fatigue crack growth, International Journal of Fracture 22 (1983) 91–104. doi:10.1007/BF00942715.
URL http://dx.doi.org/10.1007/BF00942715

[16] N. Haddar, Y. Kchaou, A. Köster, Numerical computation of the energetic criterion at isothermal and thermal–mechanical cyclic tests under generalized plasticity of the f17tnb stainless steel, Engineering Fracture Mechanics 107 (2013) 1–13.

[17] H. Bao, A. McEvily, The effect of an overload on the rate of fatigue crack propagation under plane stress conditions, Metallurgical and Materials Transactions A 26 (7) (1995) 1725–1733.

[18] M. El Haddad, K. Smith, T. Topper, Fatigue crack propagation of short cracks, Journal of Engineering Materials and Technology 101 (1) (1979) 42–46.

[19] A. Miranda, M. Meggiolaro, J. Castro, L. Martha, T. Bittencourt, Fatigue life and crack path predictions in generic 2d structural components, Engineering Fracture Mechanics 70 (10) (2003) 1259–1279.

[20] N. Simha, F. Fischer, G. Shan, C. Chen, O. Kolednik, J-integral and crack driving force in elastic–plastic materials, Journal of the Mechanics and Physics of Solids 56 (9) (2008) 2876–2895.

[21] W. Ochensberger, O. Kolednik, A new basis for the application of the j-integral for cyclically loaded cracks in elastic–plastic materials, International Journal of Fracture 189 (1) (2014) 77–101.

[22] R. P. Skelton, Energy criterion for high temperature low cycle fatigue failure, Materials Science and Technology (UK) 7 (5) (1991) 427–439.

[23] E. Charkaluk, A. Bignonnet, A. Constantinescu, K. D. Van, Fatigue design of structures under thermomechanical loadings, Fatigue & Fracture of Engineering Materials and Structures 25 (12) (2002) 1199–1206.

[24] S. Tabibian, E. Charkaluk, A. Constantinescu, F. Szmytka, A. Oudin, Tmf criteria for lost foam casting aluminum alloys, Fatigue & Fracture of Engineering Materials & Structures 36 (4) (2013) 349–360.

[25] N. Haddar, Fatigue thermique d'un acier inoxydable austénitique 304l: simulation de l'amorçage et de la croissance des fissures courtes en fatigue isotherme et anisotherme, Ph.D. thesis, Ecole des Mines de Paris (2003).

[26] R. P. Skelton, T. Vilhelmsen, G. A. Webster, Energy criteria and cumulative damage during fatigue crack growth, International Journal of Fatigue 20 (9) (1998) 641–649.

[27] D. Cojocaru, A. M. Karlsson, Assessing plastically dissipated energy as a condition for fatigue crack growth, International Journal of Fatigue 31 (7) (2009) 1154–1162.

[28] V. Maurel, L. Remy, F. Dahmen, N. Haddar, An engineering model for low cycle fatigue life based on a partition of energy and micro-crack growth, International Journal of Fatigue 31 (5) (2009) 952 – 961. doi:DOI:10.1016/j.ijfatigue.2008.09.004.
URL http://www.sciencedirect.com/science/article/B6V35-4TGXPDH-1/2/2094b0e37344864a74b3e58911ed870a

[29] É. Charkaluk, Fatigue des matériaux métalliques: quelques contributions à une approche dissipative, in french, doctoral dissertation, ecole polytechnique (2006).

[30] L. Susmel, The theory of critical distances: a review of its applications in fatigue, Engineering Fracture Mechanics 75 (7) (2008) 1706 – 1724. doi:http://dx.doi.org/10.1016/j.engfracmech.2006.12.004.
URL http://www.sciencedirect.com/science/article/pii/S0013794406004553

[31] F. Bourbita, L. Remy, A combined critical distance and energy density model to predict high temperature fatigue life in notched single crystal superalloy members, International Journal of Fatigue 84 (2016) 17–27.

[32] A. Pineau, A. Benzerga, T. Pardoen, Failure of metals i: Brittle and ductile fracture, Acta Materialia 107 (2016) 424–483.

[33] G. Rousselier, Ductile fracture models and their potential in local approach of fracture, Nuclear engineering and design 105 (1) (1987) 97–111.

[34] J. Besson, C. Guillemer-Neel, An extension of the green and gurson models to kinematic hardening, Mechanics of Materials 35 (1) (2003) 1–18.

[35] G. Pijaudier-Cabot, Z. P. Bazant, Nonlocal damage theory, Journal of engineering mechanics 113 (10) (1987) 1512–

1533.

[36] R. Peerlings, R. de Borst, W. Brekelmans, M. Geers, Localisation issues in local and nonlocal continuum approaches to fracture, European Journal of Mechanics - A/Solids 21 (2) (2002) 175 – 189. doi:10.1016/S0997-7538(02)01211-1.
URL http://www.sciencedirect.com/science/article/pii/S0997753802012111

[37] E. Lorentz, S. Andrieux, Analysis of non-local models through energetic formulations, International Journal of Solids and Structures 40 (12) (2003) 2905–2936.

[38] S. Forest, E. Lorentz, Localization phenomena and regularization methods, in: J. Besson (Ed.), Local approach to fracture, Ecole d'été "Mécanique de l'endommagement et approche locale de la rupture" (MEALOR), juillet 2004, Les presses de l'ecole des mines de paris, 2004, pp. 311–371.
URL https://hal.archives-ouvertes.fr/hal-00164479

[39] N. Saintier, T. Palin-luc, J. Bénabes, F. Cocheteux, Non local energy based fatigue life calculation method under multiaxial variable amplitude loadings, International Journal of Fatigue (0) (2013) –. doi:10.1016/j.ijfatigue.2012.12.013.
URL http://www.sciencedirect.com/science/article/pii/S0142112313000030

[40] S. Chomette, Etude des évolutions microstructurales et comportement mécanique des alliages base nickel 617 et 230 à haute température, in french, Ph.D. thesis, Institut National Polytechnique de Toulouse (2009).

[41] Y. Lu, L. Chen, G. Wang, M. Benson, P. Liaw, S. Thompson, J. Blust, P. Browning, A. Bhattacharya, J. Aurrecoechea, et al., Hold time effects on low cycle fatigue behavior of haynes 230® superalloy at high temperatures, Materials Science and Engineering: A 409 (1) (2005) 282–291.

[42] L. Chen, P. Liaw, Y. He, M. Benson, J. Blust, P. Browning, R. Seeley, D. Klarstrom, Tensile hold low-cycle fatigue behavior of cobalt-based haynes® 188 superalloy, Scripta Materialia 44 (6) (2001) 859–865.

[43] S. Lee, Y. Lu, P. Liaw, L. Chen, S. Thompson, J. Blust, P. Browning, A. Bhattacharya, J. Aurrecoechea, D. Klarstrom, Tensile-hold low-cycle-fatigue properties of solid-solution-strengthened superalloys at elevated temperatures, Materials Science and Engineering: A 504 (1) (2009) 64–72.

[44] K. B. S. Rao, M. Castelli, J. Ellis, On the low cycle fatigue deformation of haynes 188 superalloy in the dynamic strain aging regime, Scripta metallurgica et materialia 33 (6) (1995) 1005–1012.

[45] K. B. S. Rao, M. Castelli, G. Allen, J. R. Ellis, A critical assessment of the mechanistic aspects in haynes 188 during low-cycle fatigue in the range 25 c to 1000 c, Metallurgical and Materials Transactions A 28 (2) (1997) 347–361.

[46] Y. Lu, High-temperature low-cycle-fatigue and crack-growth behaviors of three superalloys: Hastelloy® x, haynes® 230, and haynes® 188.

[47] S. Lee, Y. Lu, P. K. Liaw, H. Choo, S. A. Thompson, J. W. Blust, P. F. Browning, A. K. Bhattacharya, J. M. Aurrecoechea, D. L. Klarstrom, Elevated-temperature creep-fatigue crack-growth behavior of haynes® 188 superalloy, in: Key Engineering Materials, Vol. 345, Trans Tech Publ, 2007, pp. 287–290.

[48] S. Lee, Y. Lu, P. Liaw, H. Choo, S. Thompson, J. Blust, P. Browning, A. Bhattacharya, J. Aurrecoechea, D. Klarstrom, High-temperature tensile-hold crack-growth behavior of hastelloy® x alloy compared to haynes® 188 and haynes® 230® alloys, Mechanics of Time-Dependent Materials 12 (1) (2008) 31–44.

[49] G. R. Halford, Cumulative fatigue damage modeling?crack nucleation and early growth, International Journal of Fatigue 19 (93) (1997) 253–260.

[50] J. L. Chaboche, F. Gallerneau, An overview of the damage approach of durability modelling at elevated temperature, Fatigue & Fracture of Engineering Materials and Structures 24 (6) (2001) 405–418.

[51] M. Reger, L. Remy, High temperature, low cycle fatigue of in-100 superalloy ii: influence of frequency and environment at high temperatures, Materials Science and Engineering: A 101 (1988) 55–63.

[52] R. Neu, H. Sehitoglu, Thermomechanical fatigue, oxidation, and creep: Part ii. life prediction, Metallurgical Transac-

tions A 20 (9) (1989) 1769–1783.

[53] J. Reuchet, L. Remy, Fatigue oxidation interaction in a superalloy. application to life prediction in high temperature low cycle fatigue., Metallurgical Transactions A 14A (1983) 141–149.

[54] A. Koster, Fatigue thermique d'un alliage pour aubes de turbopompe astronautique: le superwaspaloy (in french), Ph.D. thesis, École Nationale Supérieure des Mines de Paris (1997).

[55] E. Chateau, L. Remy, Oxidation-assisted creep damage in a wrought nickel-based superalloy: Experiments and modelling, Materials Science and Engineering A 527 1655 – 1664.

[56] K. S. Chan, P. Jones, Q. Wang, Fatigue crack growth and fracture paths in sand cast b319 and a356 aluminum alloys, Materials Science and Engineering: A 341 (1) (2003) 18–34.

[57] X. Wang, F. Liang, J. Fan, F. Zhang, Low-cycle fatigue small crack initiation and propagation behaviour of cast magnesium alloys based on in-situ sem observations, Philosophical Magazine 86 (11) (2006) 1581–1596.

[58] E. Heripre, M. Dexet, J. Crepin, L. Gelebart, A. Roos, M. Bornert, D. Caldemaison, Coupling between experimental measurements and polycrystal finite element calculations for micromechanical study of metallic materials, Int. J. Plast. 23 (9) (2007) 1512–1539. doi:{10.1016/j.ijplas.2007.01.009}.

[59] R. Pippan, W. Grosinger, Fatigue crack closure: from lcf to small scale yielding, International Journal of Fatigue 46 (2013) 41–48.

[60] M. A. Sutton, J. Yan, X. Deng, C.-S. Cheng, P. Zavattieri, Three-dimensional digital image correlation to quantify deformation and crack-opening displacement in ductile aluminum under mixed-mode i/iii loading, Optical Engineering 46 (5) (2007) 051003–051003.

[61] J. Réthoré, F. Hild, S. Roux, Extended digital image correlation with crack shape optimization, International Journal for Numerical Methods in Engineering 73 (2) (2008) 248–272.

[62] V. A. Esin, V. Maurel, P. Breton, A. Koster, S. Selezneff, Increase in ductility of pt-modified nickel aluminide coating with high temperature ageing, Acta Materialia 105 (2016) 505 – 518. doi:http://dx.doi.org/10.1016/j.actamat.2015.12.008.
URL http://www.sciencedirect.com/science/article/pii/S1359645415301166

[63] F. Salgado-Goncalves, A. Koster, V. Maurel, L. Remy, Growth and interaction of cracks nucleated from multiple holes under high temperature fatigue from small to large scale yielding, 4th International Conference on "Crack Paths" (CP 2012) Gaeta, Italy, 19 - 21 September, 2012.

[64] F. Salgado Goncalves, Caractérisation expérimentale et modélisation des interactions entre fissures et perçages multiples à haute température en élastoplasticité généralisée ou confinée, Ph.D. thesis, Mines ParisTech (2013).

[65] F. Salgado-Goncalves, L. Remy, A. Koster, V. Maurel, Interaction of micro-cracks under large scale yielding at high temperature, In preparation).

[66] NF, NF A03-400, Produits sidérurgiques - Essais de fatigue - Principes généraux, AFNOR, 1983.

[67] ASTM, ASTM E 647, Standard test method for measurement of fatigue crack growth rates, Vol. 88A, 03.01, ASTM International, 1990.

[68] F. Soniak, L. Remy, Fatigue growth of long and short cracks in a powder metallurgy nickel base superalloy, in: K. Miller, E. de los Rios (Eds.), The Behavior of Short Fatigue Cracks, EGF Pub. 1„ Mechanical Engineering Publications, London, 1986, pp. 133–142.

[69] A. Defresne, L. Remy, Fatigue behaviour of cmsx 2 superalloy [001] single crystals at high temperature ii: Fatigue crack growth, Materials Science and Engineering A 129 (1) (1990) 55–64.

[70] J. Grison, L. Remy, Fatigue failure probability in a powder metallurgy ni-base superalloy, Engineering Fracture Mechanics (UK) 57 (1) (1997) 41–55.

[71] A. Koster, E. Fleury, E. Vasseur, L. Remy, Thermal-mechanical fatigue testing. in: Automation in fatigue and fracture:

Testing and analysis (edited by c. amzallag), ASTM STP 1231 (1994) 563–580.

[72] G. Besnard, F. Hild, S. Roux, 'finite-element' displacement fields analysis from digital images: Application to portevin-le chatelier bands, Experimental Mechanics 46 (6) (2006) 789–803.

[73] V. Maurel, L. Remy, M. Harvey, H. Tezenas du Montcel, A. Koster, The respective roles of thermally grown oxide roughness and nial coating anisotropy in oxide spallation, Surface and Coatings Technology 215 (2013) 52 – 61. doi:10.1016/j.surfcoat.2012.08.097.
URL http://www.sciencedirect.com/science/article/pii/S025789721201105X

[74] G. Chalant, L. Remy, A metallographic method for determining plastic strains at the tip of a fatigue crack, Materials Science and Engineering 50 (2) (1981) 253–261.

[75] F. Hourlier, D. McLean, A. Pineau, Fatigue crack growth behaviour of ti-5al-2· 5sn alloy under complex stress (mode i+ steady mode iii), Metals Technology 5 (1) (1978) 154–158.

[76] V. Lazarus, J.-B. Leblond, S.-E. Mouchrif, Crack front rotation and segmentation in mixed mode i+ iii or i+ ii+ iii. part ii: Comparison with experiments, Journal of the Mechanics and Physics of Solids 49 (7) (2001) 1421–1443.

[77] J. Besson, R. Foerch, Large scale object-oriented finite element code design, Comp. Methods Appl. Mech. Engrg. 142 (1997) 165–187.

[78] D. Benziane, V. Chiaruttini, J. Garaud, F. Feyel, R. Foerch, N. Osipov, S. Quillici, J. Rannou, A. Roos, D. Ryckelynck, Z-set/zebulon: une suite logicielle pour la mécanique des matériaux et le calcul de structures, Comptes rendus du 10ème Colloque National en Calcul des Structures, Giens, 2011.

[79] Zset software, non-linear material & structure analysis suite, http://www.zset-software.com.

[80] S. Declercq, Tech. rep., Snecma - Groupe Safran (1999).

[81] S. Otin, Lois d'endommagement incrementales isotrope/anisotropes pour applications thermomécaniques complexes, Ph.D. thesis, École normale supérieure de Cachan-ENS Cachan (2007).

[82] R. Desmorat, S. Otin, Cross-identification isotropic/anisotropic damage and application to anisothermal structural failure, Engineering Fracture Mechanics 75 (11) (2008) 3446–3463.

[83] J.-L. Chaboche, A. Gaubert, P. Kanouté, A. Longuet, F. Azzouz, M. Mazière, Viscoplastic constitutive equations of combustion chamber materials including cyclic hardening and dynamic strain aging, International Journal of Plasticity 46 (2013) 1–22.

[84] F. Szmytka, P. Michaud, L. Remy, A. Köster, Thermo-mechanical fatigue resistance characterization and materials ranking from heat-flux-controlled tests. application to cast-irons for automotive exhaust part, International Journal of Fatigue 55 (2013) 136–146.

[85] J. Besson, C. McCowan, E. Drexler, Modeling flat to slant fracture transition using the computational cell methodology, Engineering Fracture Mechanics 104 (2013) 80–95.

[86] T. Morgeneyer, J. Besson, Scripta Materialia 65 (11) (2011) 1002 – 1005. doi:10.1016/j.scriptamat.2011.09.004, [link].
URL http://www.sciencedirect.com/science/article/pii/S1359646211005306

[87] S. Dezecot, J.-Y. Buffiere, A. Koster, V. Maurel, F. Szmytka, E. Charkaluk, N. Dahdah, A. El Bartali, N. Limodin, J.-F. Witz, In situ 3d characterization of high temperature fatigue damage mechanisms in a cast aluminum alloy using synchrotron x-ray tomography, Scripta Materialia 113 (2016) 254–258.

[88] S. Dezecot, V. Maurel, J.-Y. Buffiere, F. Szmytka, A. Koster, 3d characterization and modeling of low cycle fatigue damage mechanisms at high temperature in a cast aluminum alloy, Acta Materialia 123 (2017) 24–34.

[89] E. Ferrié, J.-Y. Buffiere, W. Ludwig, A. Gravouil, L. Edwards, Fatigue crack propagation: In situ visualization using x-ray microtomography and 3d simulation using the extended finite element method, Acta Materialia 54 (4) (2006) 1111–1122.

[90] S. Pommier, A. Gravouil, N. Moes, A. Combescure, Extended finite element method for crack propagation, John Wiley & Sons, 2013.

[91] V. Chiaruttini, D. Geoffroy, V. Riolo, M. Bonnet, An adaptive algorithm for cohesive zone model and arbitrary crack propagation, European Journal of Computational Mechanics/Revue Européenne de Mécanique Numérique 21 (3-6) (2012) 208–218.

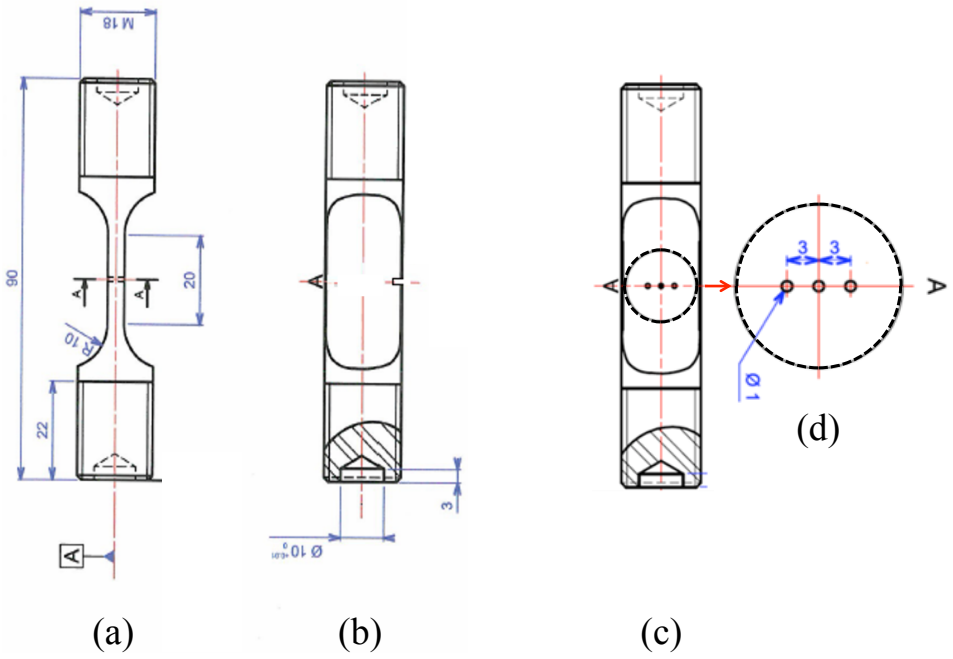

Figure 1: Specimens used for crack growth (a) side view common for both SENT and 3-holes specimens ; (b) SENT specimen ; (c) 3-holes specimen; (d) detailed view of three holes; dimensions are given in mm

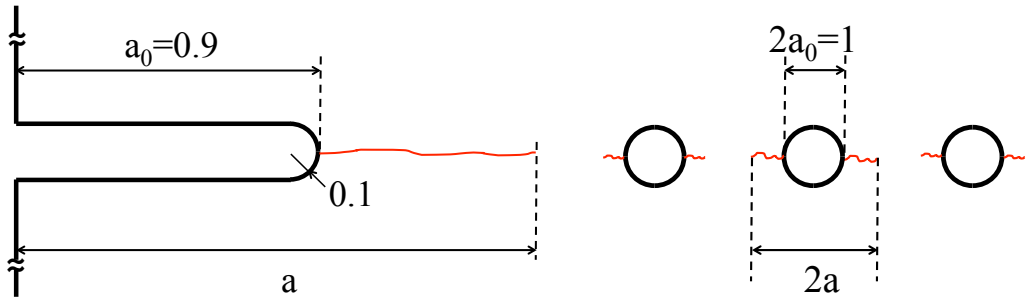

(a) SENT specimen (b) 3-holes specimen

Figure 2: Optical crack growth measurement method, where a_0 corresponds to the notch length and the hole radius respectively ; dimensions are given in mm

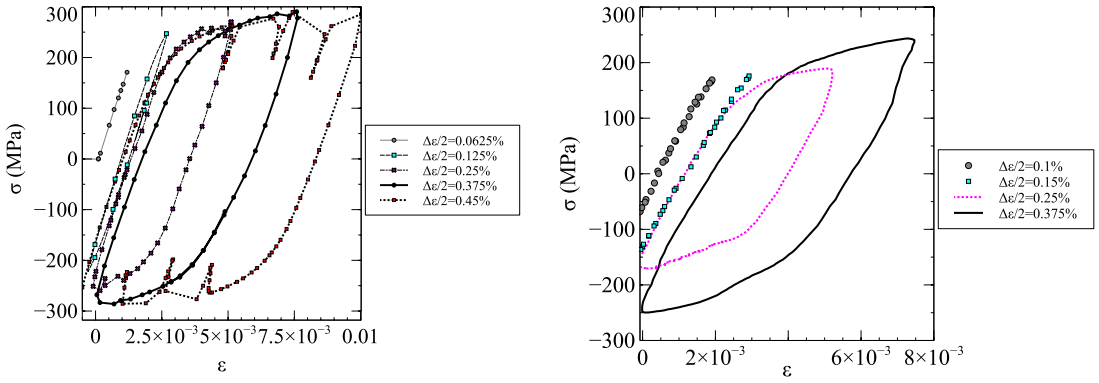

(a) SENT test series (b) 3-holes test series

Figure 3: Stress-strain evolution at $N/N_{\max} = 0.2$

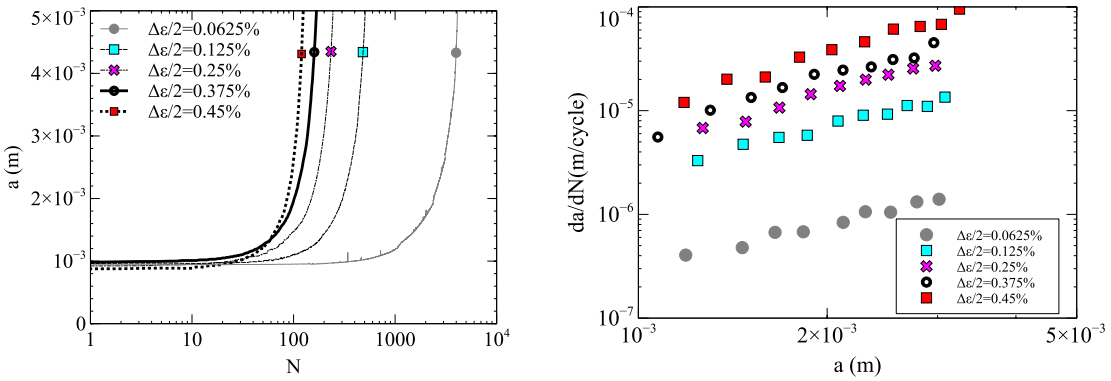

(a) Crack length as a function of the number of cycle (b) Crack growth rate as a function of the crack length

Figure 4: Evolution of measured (a) crack length and (b) derived crack growth rate for SENT test series

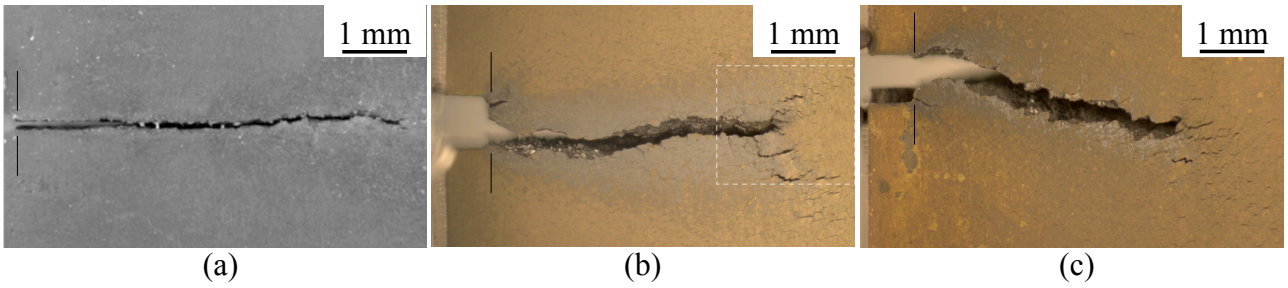

Figure 5: Crack path for SENT specimen for (a) $\Delta\varepsilon/2 = 0.0625\%$, (b) $\Delta\varepsilon/2 = 0.25\%$ and (c) $\Delta\varepsilon/2 = 0.45\%$ tests with $R_\varepsilon = 0$ close to the end of the test ($a \simeq 5$ mm). Vertical lines indicate the horizontal location of the frontier between the notch and the crack. Dashed rectangle corresponds to detailed Figure 7.

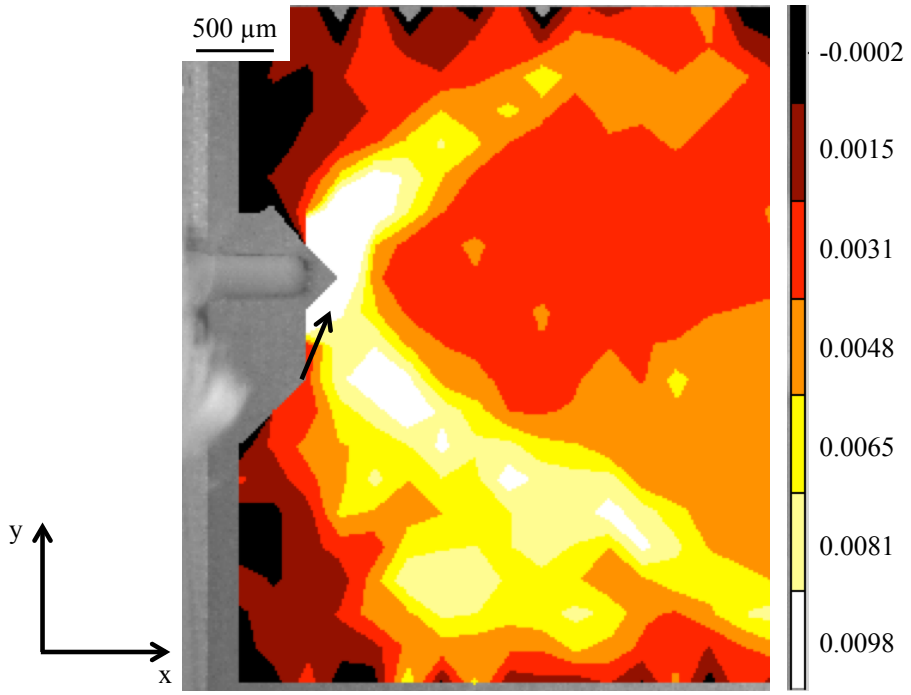

Figure 6: Strain field, component ε_{yy}, measured on surface for SENT specimens for $\Delta\varepsilon/2 = 0.25\%$, $R_\varepsilon = 0$, test

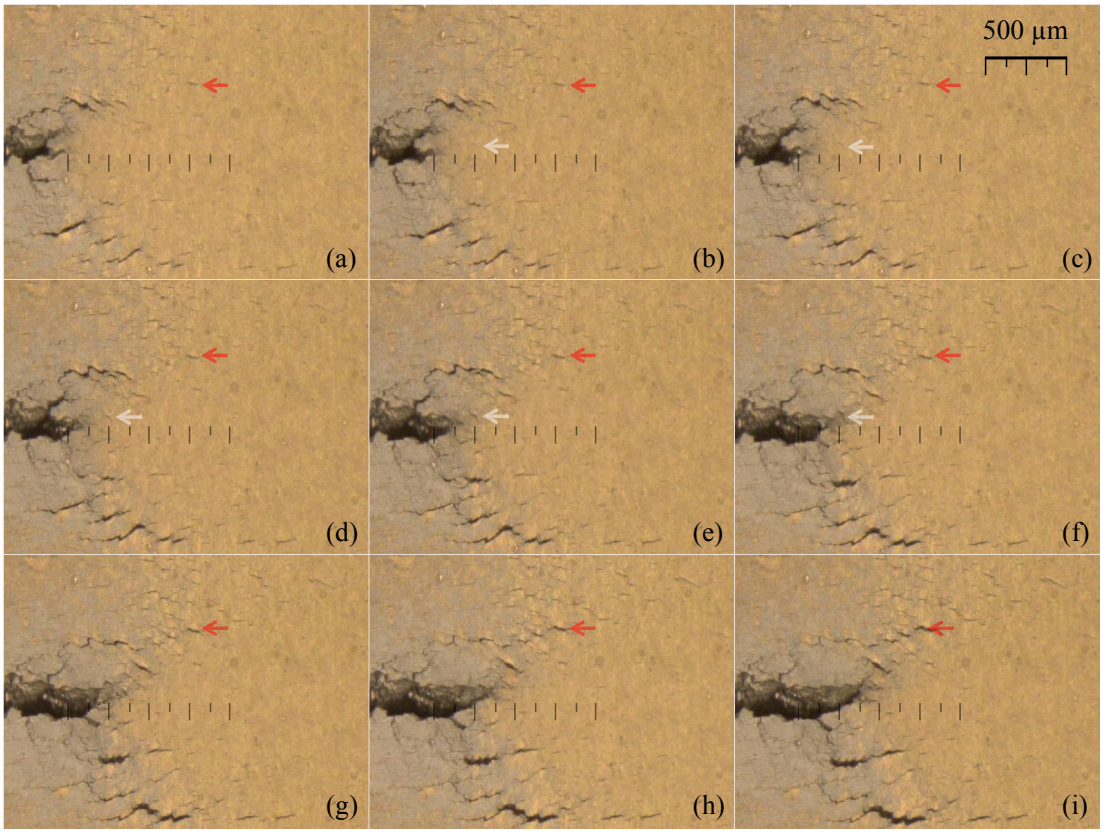

Figure 7: Details of crack growth for SENT specimen for $\Delta\varepsilon/2 = 0.25\%$ with $R_\varepsilon = 0$. Each image from (a) to (i) corresponds to maximum strain loading of cycles 248 to 256. The region of interest corresponds to the dashed rectangle in figure 5(b). (A scale is inserted with vertical lines for easiness of reading).

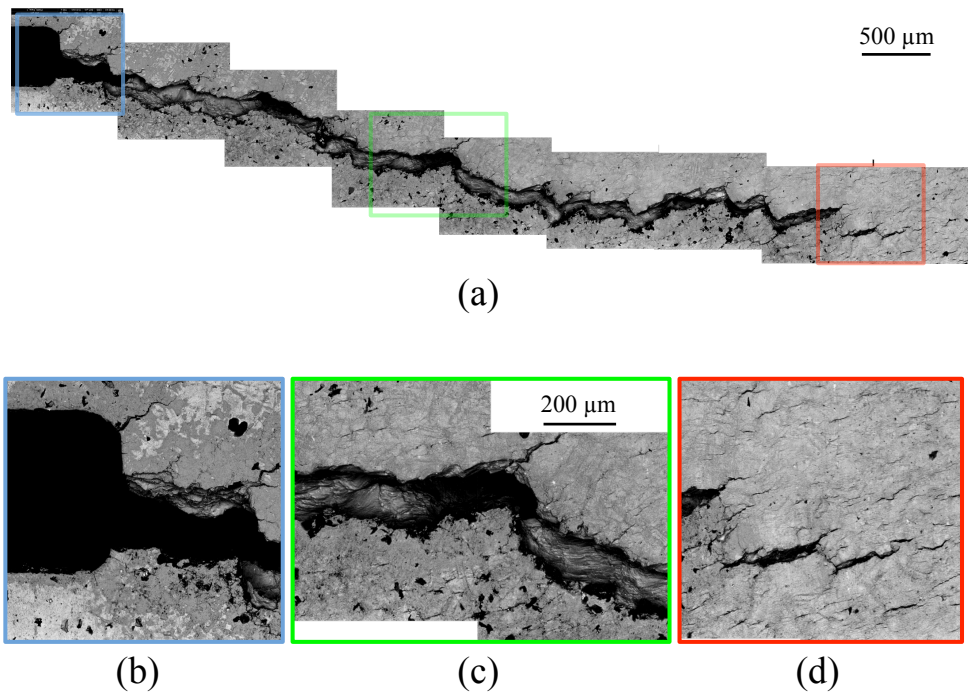

Figure 8: Crack path for SENT specimen for test $\Delta\varepsilon/2$= 0.45%, $R_\varepsilon = 0$ observed by SEM using BSE mode. Color highlights in (a) correspond to details in (b), (c) and (d)

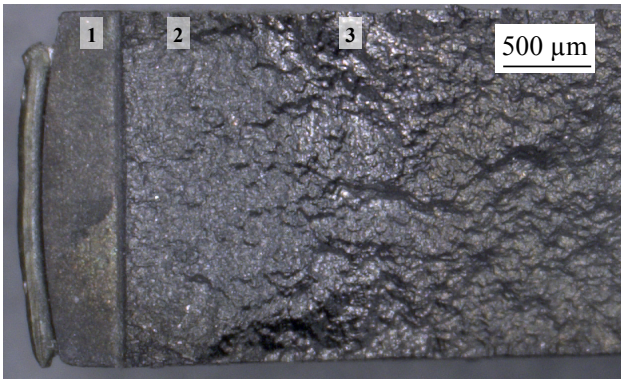

(a) Optical microscope

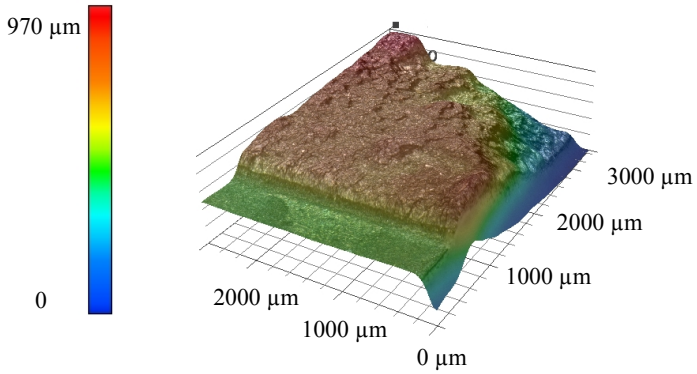

(b) Roughness measurement

Figure 9: Fracture surface for $\Delta\varepsilon/2$= 0.45%, $R_\varepsilon = 0$ test for SENT specimen.

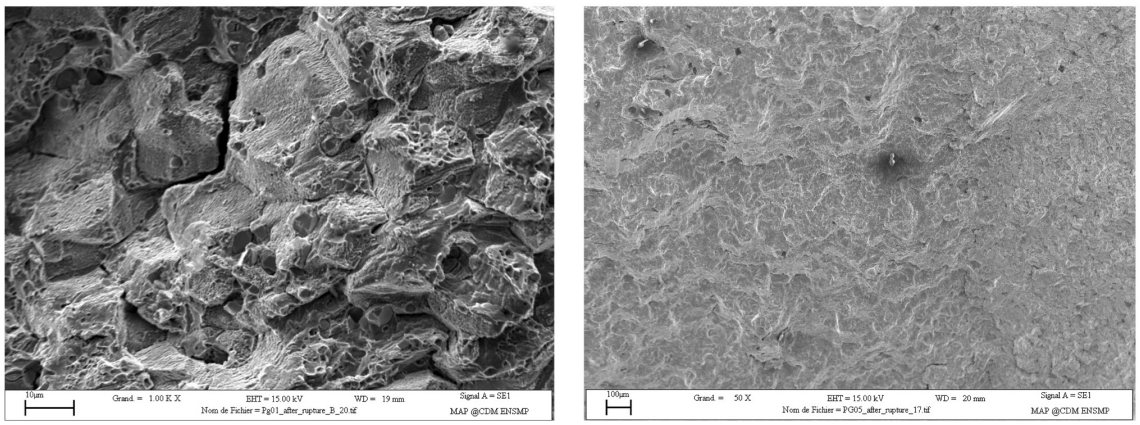

Figure 10: Fracture surface observation for SENT specimen for (a) $\Delta\varepsilon/2 = 0.25$ and (b) $\Delta\varepsilon/2 = 0.45$, tests (see Table 2)

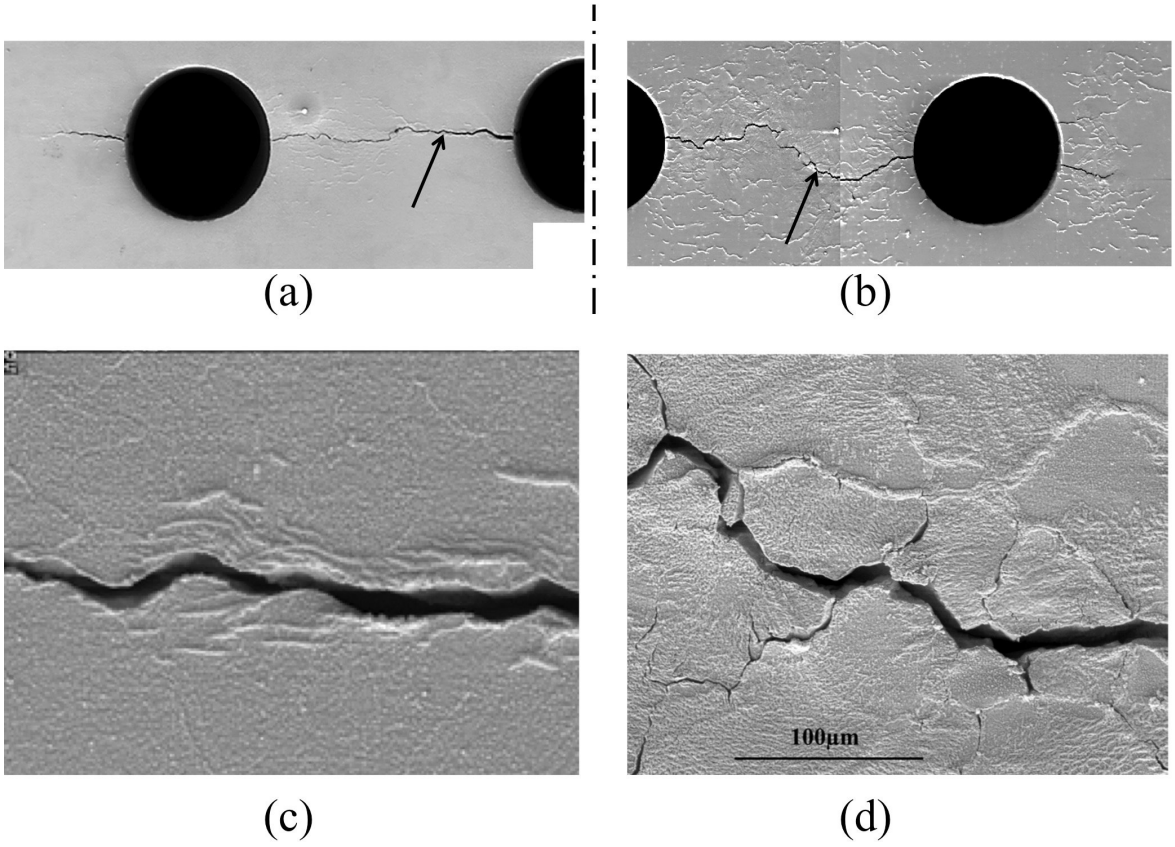

Figure 11: Crack path for three holes specimen for (a) $\Delta\varepsilon/2 = 0.1\%$, $R_\varepsilon = 0$, test ; and (b) $\Delta\varepsilon/2 = 0.375\%$, $R_\varepsilon = 0$, test. Zoom (c) corresponds to black arrow in figure (a) and zoom (d) corresponds to black arrow in figure (b). Dashed line indicates the location of the symmetry plane of the specimen.

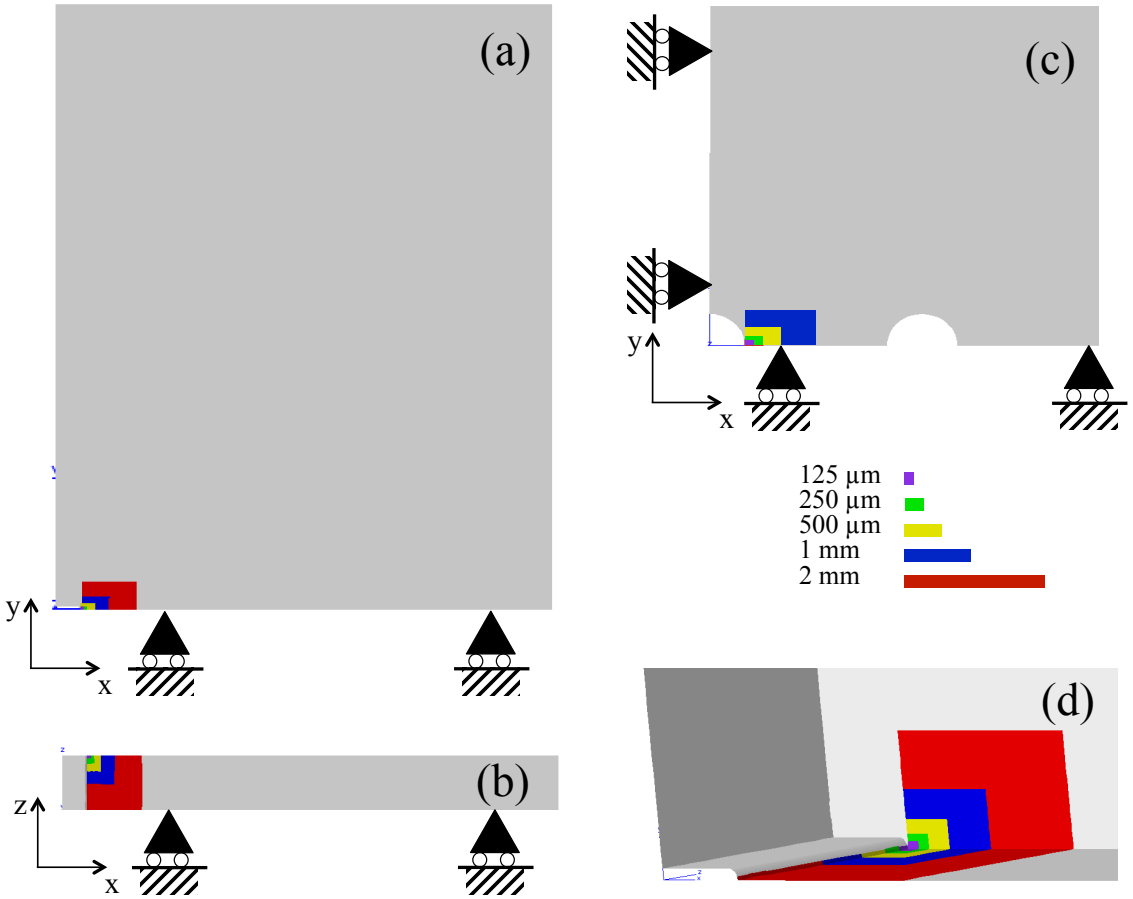

Figure 12: Boundary conditions and boxes used for numerical evaluation of w_e and w_p for (a) (xy) plane and (b) (zx) plane for SENT specimens and (c) (xy) plane for three holes specimens; (d) detailed perspective view of notch and associated boxes for SENT specimen; the boxes are tangent to both notch and free surface of the specimen. The color legend indicates the size of the boxes along x direction, boxes are cubic considering symmetry of the problem.

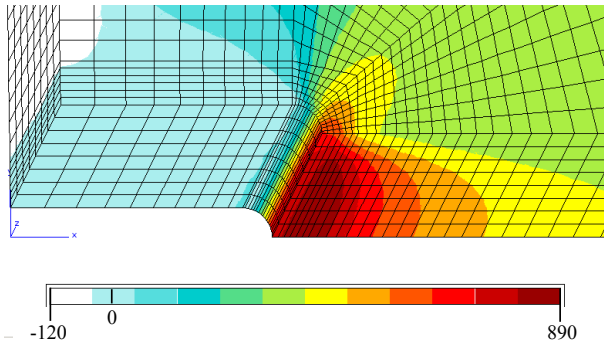

(a) Stress evolution σ_{yy}(MPa)

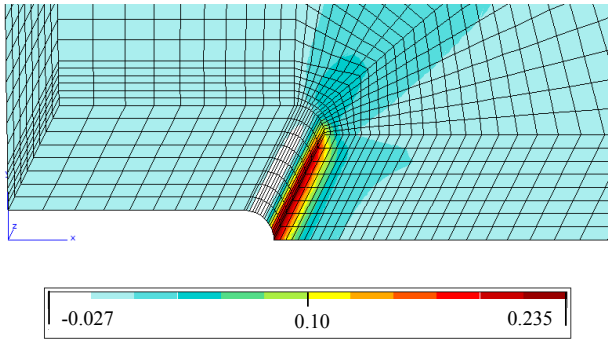

(b) Total strain ε_{yy}^{tot}

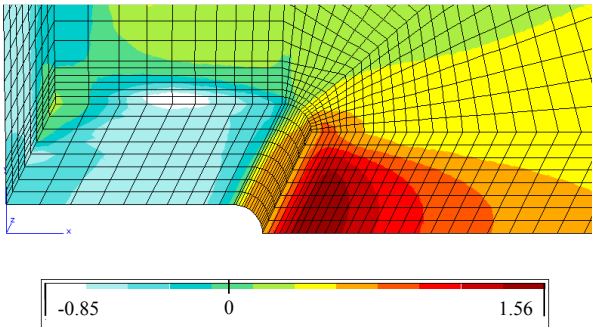

(c) Stress triaxiality

Figure 13: Stress and strain fields for SENT specimen for $\Delta\varepsilon/2 = 0.375\%$

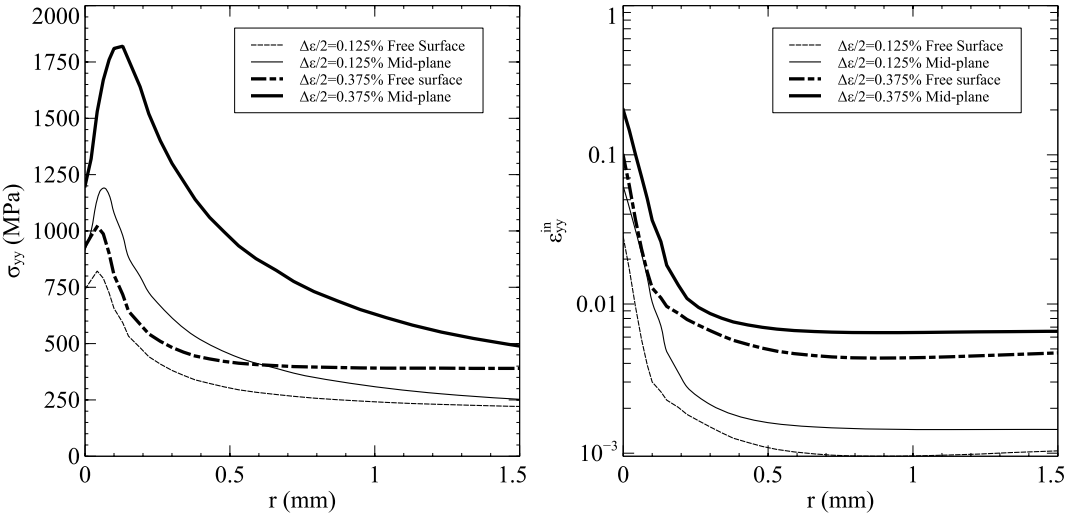

(a) Stress evolution σ_{yy}

(b) Inelastic strain ε_{yy}

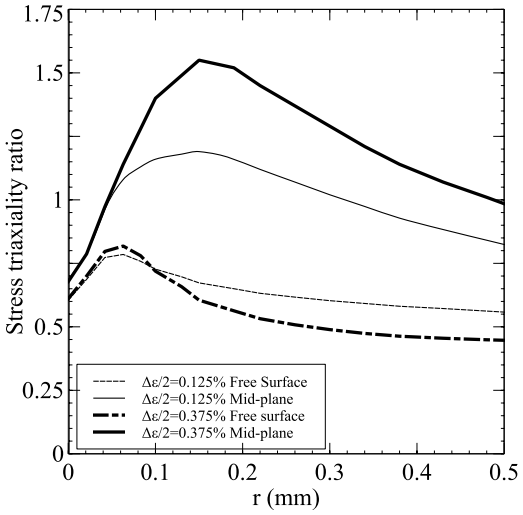

(c) Stress triaxiality

Figure 14: Evolution of out-of-plane stress, inelastic strain and stress triaxiality ratio for SENT specimen as a function of the distance to the notch root r ; $z = 0$ corresponds to the mid-plane and $z = 2$ to the free surface of the specimen

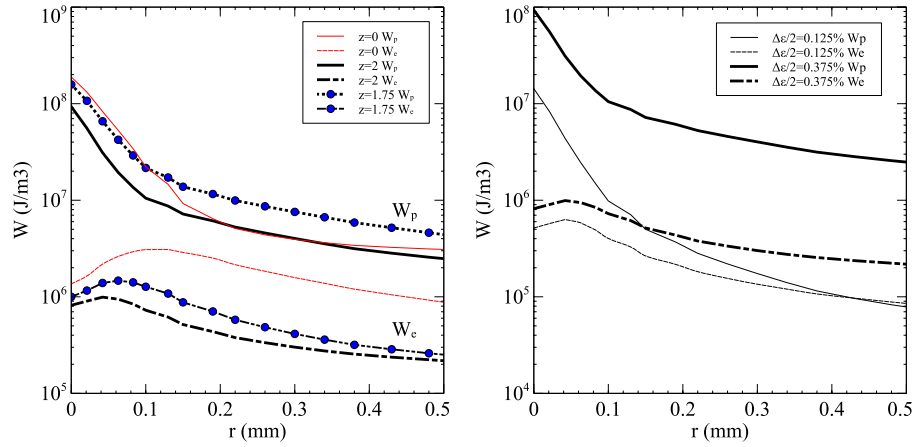

(a) Influence of the location through specimen thickness z for $\Delta\varepsilon/2 = 0.375\%$

(b) Influence of the applied strain for $z = 2$ mm (specimen free surface)

Figure 15: Energy evolution for SENT specimen as a function of the distance to the notch root r ; $z = 0$ corresponds to the mid-plane and $z = 2$ to the free surface of the specimen.

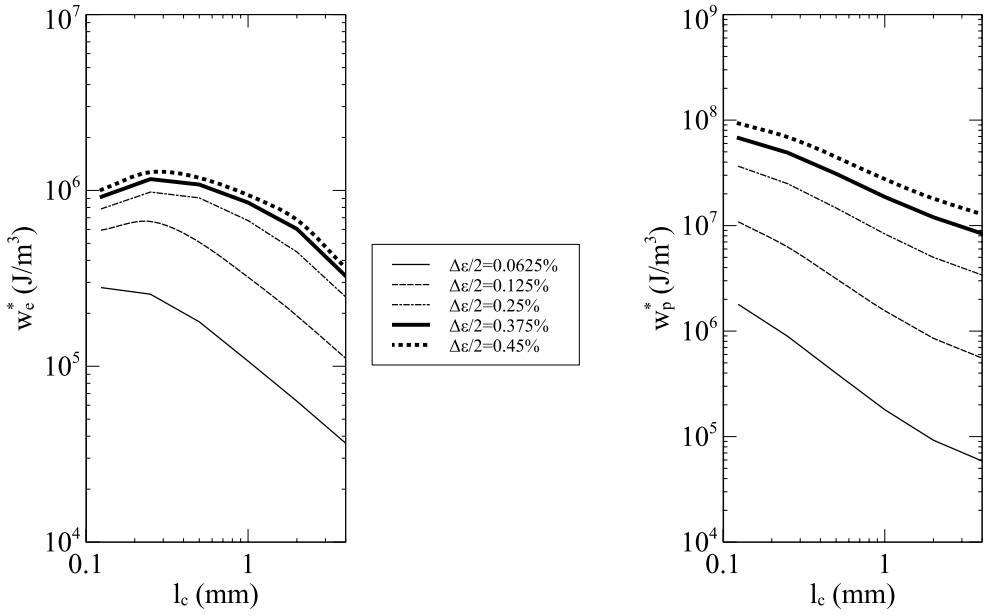

(a) w_e^*

(b) w_p^*

Figure 16: Evolution of energies w_e^* and w_p^* as a function of the average box size l_c

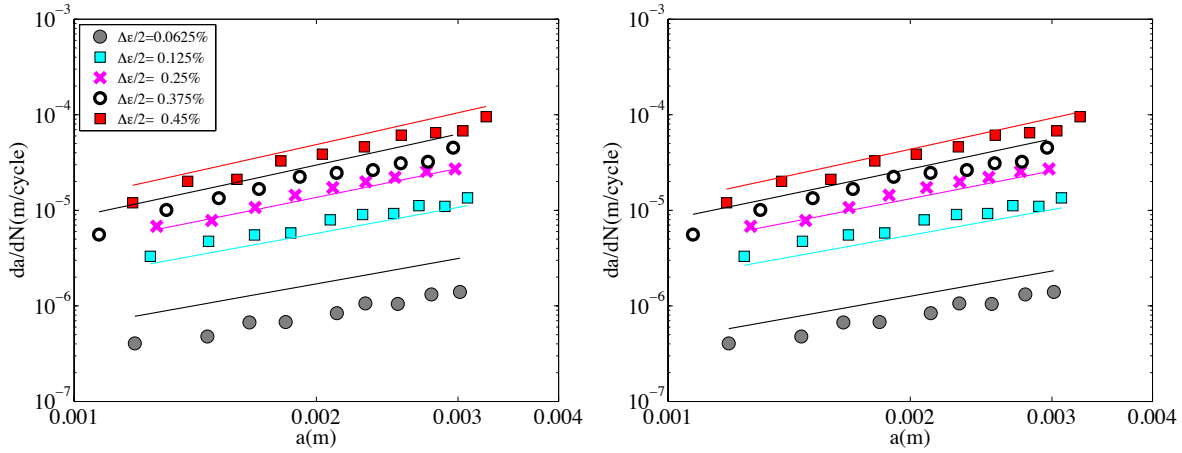

(a) $l_c = 125$ μm

(b) $l_c = 250$ μm

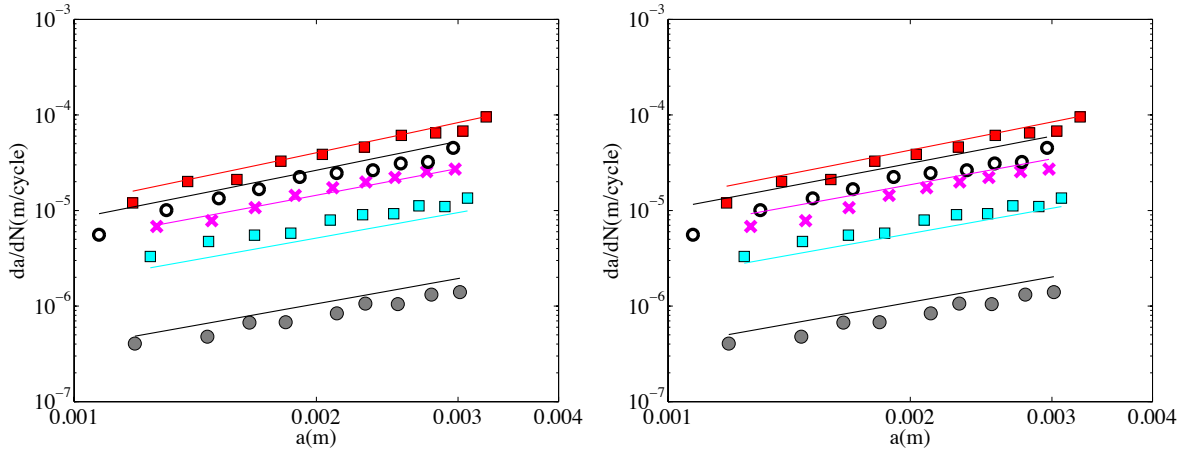

(c) $l_c = 500$ μm

(d) $l_c = 1$ mm

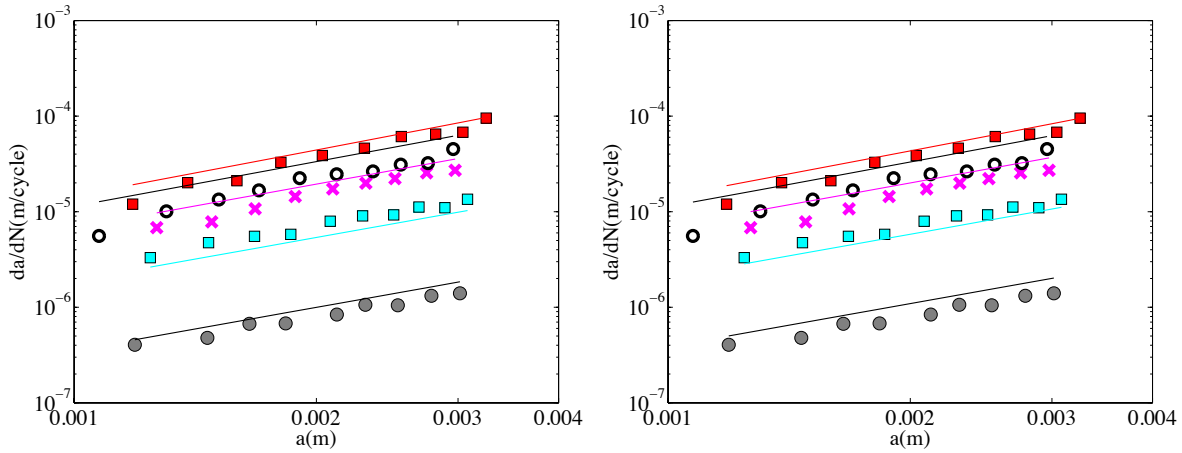

(e) $l_c = 2$ mm

(f) $l_c = 4$ mm

Figure 17: Modeling of crack growth rate as a function of the box size, l_c, for SENT specimens

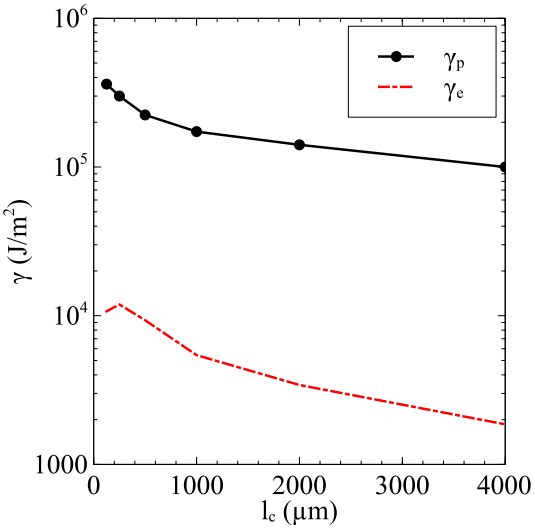

Figure 18: Evolution of γ_e and γ_p model parameters as a function of the box size for SENT specimens

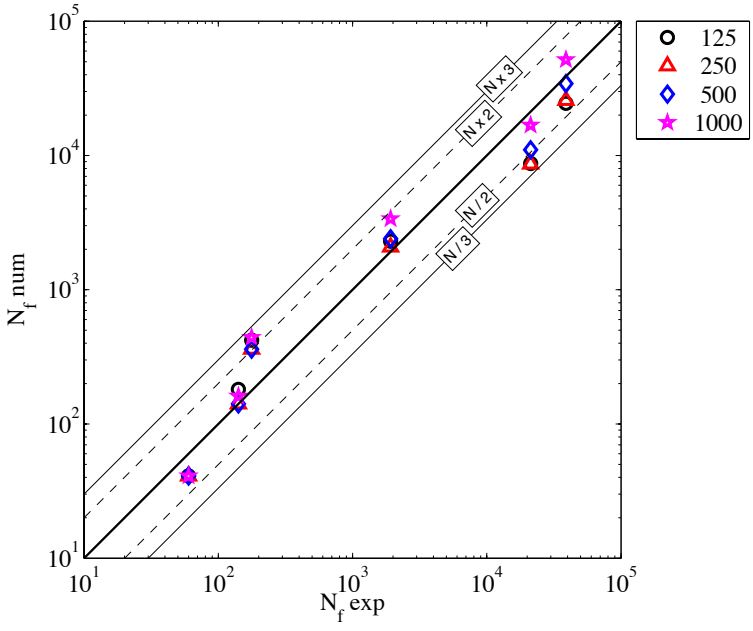

Figure 19: Comparison between the modeled (Nf num) and the experimental (Nf exp) number of cycles to reach a_f as a function of the box size for three holes specimens; the legend indicates the characteristic length of the box size given in μm; dashed lines and thin lines correspond respectively to a factor of two and three above and below experimental observation